Author's response to reviewers:

P. Carbonneau (Referee #1):

5 **General Comments**

This work attempts to deploy established SfM techniques over a 1.2 km river bank characterised by bays and pseudo-headlands and with numerous vertical faces along the banks. The work does present some points of interest but the authors display an understanding of SfM-photogrammetry which is average/good and as a result seem to have missed many important points. The general pitch and justification of novelty for this paper is weak. This is expressed in the second

10 sentence of the abstract stating 'Yet, no technique provides low-cost and high-resolution to survey small-scale bank processes along a river reach'. This is quite simply not true and is ultimately self-defeating as a statement. The authors have deployed a widely used commercial drone and processed the data with an equally widely used commercial SfM package using the standard workflow. There is no new technique in this work. The authors have cited other work that has delivered similar resolutions at slightly smaller scales or that have worked at lower resolutions at larger scales. Therefore the work

15 occupies a very small niche of cm scale resolution work over a 1.2km scale length. The workflow and techniques used by the authors are not at all new, they have merely benefited from better drone flight durations thus allowing them to cover a 1.2km river reach with repeated operations. In itself, this is not a sufficient justification for publication. However, the work does address an important and interesting problem. Using drone-based SfM for repeated coverage of a 1km river corridor, especially a very linear one as shown here, presents some very specific challenges. Moreover, when this reach presents some

20 vertical surfaces prone to failure, additional photogrammetric challenges must be addressed. Unfortunately, the authors did not seem to realise that this was the key point and challenge of their work and, in addition to the misplaced pitch mentioned above, the data acquisition and processing approach is very sub-optimal for this specific problem.

Overall, I do think the data presented here has potential for publication without additional fieldwork, but some very significant revisions will be required which include both new analysis and re-writes of many sections. However, even if

25 publishable without additional fieldwork, the workflow presented here is definitely not the optimal approach to survey long and highly linear river corridors and this will need to be clearly outlined in a new discussion.

> We thank the referee for his critical and constructive comments on the UAV-SfM technique, which has helped improving the manuscript and the analysis of the specific challenges this case study proposes for the UAV-SfM application.

30 > The manuscript addresses two aspects which have been clarified and considered in the revised analysis. First, the application of an available technique to a new setting with particular characteristics and processes. The topography of the bank area has an unusual three-dimensional complexity, it is tortuous and presents exposed undermined profiles, which overall lays on a quasi-linear domain, i.e., a straight river reach. We were aware of the latter but

1

certainly did not address it as a novelty nor analysed the rotational tendency of the model. Second, the work provides evidence of a sufficiently accurate data acquisition approach to measure bank erosion processes, without the intention of achieving an optimal solution. Yet, we do realize that this should be thoroughly discussed in the manuscript in light of the referee's comments. In addition, the fact that now it is clear for us that the SfM camera calibration phase cannot re-adjust the linear transformation, provided the opportunity to improve the manuscript towards recommending a more robust UAV-SfM approach, as well as analysing and highlighting the particular challenges this setting offered for the UAV-SfM application.

We also realize that the pitch was not accurate and should be phrased again. The spirit of the motivation lays on the application of a readily available technique to measure bank erosion at the process scale, which has unique characteristics compared to previously used methods for that aim, such as a combination of low-cost, fast deployment in the field, and high 3D resolution. Section 2.2 described past experiences with other techniques. Moreover, we compared the results with other two methods and discussed them in the broader context of other available techniques to put into perspective the convenience and disadvantages of UAV-SfM to measure bank erosion processes. We have, nevertheless, also focused the manuscript on the specific challenges this case study proposes for the UAV-SfM technique, addressing the rotational tendency of such linear domain, and assessing the performance of the adopted GCP distribution with parallel UAV paths.

Specific Comments

The key challenge in this work is the deployment of drone-based SfM over a very linear river reach characterised with near-vertical faces. This challenge can be understood if we consider the type of errors present in SfM point clouds. This is the main area where the authors understanding of SfM needs to improve. The error of georeferenced point clouds produced from SfM chan be partitionned in linear, non-linear and random components. Linear errors affect the point cloud as a rigid block and can be expressed in terms of translation errors, rotation errors and scaling errors. Non-linear errors are often caused by camera calibration problems and are manifest by warps and curvature effects that distort the geometry of the point cloud. One notable error in the authors understanding is that the seem to think that camera calibration errors can cause overall rotation of the block as 1 rigid body. This is not the case. Camera calibration errors cause errors such as the now famous dish effect. However rigid block rotation errors are caused by errors in the 7-parameter Helmert transform used to scale, rotate and translate a relative point cloud to georeferenced coordinates. The parameters of the Helmert transform are calculated by least squares regression of the control data, if the control data is highly co-linear, the lest squares regression could converge on a false solution that is rotated around the axis formed by the line of control points. This is not the same as the non-linear camera calibration errors. It is also different from random errors are localised errors (often expressed as elevation errors) that are generally not spatially correlated and represent the classic concept of precision. In this work, the authors have been rigorous about possible effects of camera calibration and small scale noise, but they have completely missed possible rotation errors caused by the geometry of their case study.

From a photogrammetric perspective, there are 2 challenges posed by this case study. First, it is a highly linear reach with a very high length:width ration. Second, the presences of vertical faces will require highly oblique views. It is the first challenge that the authors have missed. There are 2 main problems in the data acquisition plan. First, the location of the GCPs is almost co-linear. As stated above,this means that numerical solutions to the georeferencing of the model (via the Helmert transform) will have a degree of equifinality around a family of solutions that rotate around this co-linear axis of GCP points. The addition of 2-3 points perhaps 50 meters inland would have reduced the co-linearity of the model. The authors need to consider the cross-stream footprint of their GCP points relative to the errors in the RTK GPS and in the human error associated to locating the GCP in an image (see below) and make a case that the model is stable. In the future, the authors must seek to distribute their GCPs in a very non-colinear pattern that, as much as possible, occupies the full X, Y and Z extent of the area covered by imagery. Second, the choice of flight patterns that are lines parallel to the shore does not help this situation. A possible option would have been to fly the drone in a much wider pattern that goes further inland and off-shore. However, in this case, the relatively high error of the drone GPS would have required a fairly wide (in the cross-stream direction) flight pattern in order for the drone GPS data to make a beneficial contribution to the rotational stability of the model. Ultimately, the entire data acquisition setup proposed here is prone to delivering models that will have a tendency to present rotation errors where the entire point model is tilted with respect to an axis that is parallel to the shore line. This is a very significant weakness of this workflow. With this consideration in mind, it is very worrying that the authors have chosen to cut the data and have selected a portion of the point cloud that is near the GCP axis. In figure 7, the authors need to show the readers all the available data. Additionally, if they do choose to cut some peripheral data, some objective criteria must be chosen. And the moment, the choice of area seems subjective and does not give the reader confidence that the authors have not cherry-picked the part of their point cloud with the least error. I note that in figure 9, cross sections 1,2 and 4 do seem to have a rotational effect. The authors will need to demonstrate their current GCP setup does prevent rotation or return to the field with a better, wider GCP arrangement.

As previously indicated, we assumed it was possible to re-adjust the linear transformation during the camera calibration step, and missed an analysis of possible rotation errors.

We have added a new section 4.3 to analyse the linear rotation of the model, evaluating linear trends of elevation errors across the axis of potential rotation. We also included discussions on linear errors in section 5.1 and on the adopted workflow on a new section 5.3, including considerations on GCP distribution, target visualization and UAV paths.

Regarding Figure 7, the cropping of the floodplain boundary was done to avoid the bush lines across the floodplain (visible in the background aerial photo) to prevent comparisons over vegetated areas. Also, the domain had been cropped at the terrace end, before a narrow sloped strip because it was considered beyond the target area (the bank). Now, all available data has been plotted in the revised Figure 7 (whose extent was already visible in Figure 3). In addition, Figure 7 now has another panel showing the signed elevation differences between SfM and ALS for further analyses.

3

The new Section 4.3 shows that there is a slight model rotation, resulting in an absolute elevation difference between the least and most retreated bank scarps of 4 cm. This has been discussed in Section 5.1 in the context of the other error sources. Also, the new Section 5.3 discusses the adopted workflow and recommends improvements for future works.

5   The magnitude of the model rotation cannot be appreciated in the metre scale of Figures 9 and 10. These Figures show that the DSM was sufficiently accurate to measure bank erosion processes. This implies both sufficient accuracy and resolution at the bank area to quantify the three phases of the erosion cycle and the respective processes. We have added a quantitative reference to assess the performance of the method in this regard.

10   **Technical corrections:**

Abstract. Whilst Westoby et al 2012 did use hyphens when writing Structure-from-motion, this is an error . In the computer vision domain, where SfM was invented, hyphens are not used and so it is corectly written as Structure from Motion.

The hyphens have been removed in all sections.

Section 2.2 This section does not cover the needed material to adress this case study. Need more on GCP distribution and on
15   how a point cloud is georefenrenced. See Fonstad et al 213 or Carbonneau and Dietrich 2017 (both aldready cited) for details

An explanation of the particular challenges of this case study for SfM has been added in Section 2.2. Also, a description of error sources and model georeferentiation has been added to Section 3.3.

P7 line 7. By default, Cloud Compare computes differences along the Z axis. Did you use the M3C2 module which computes differences along the surface normals? Please clarify.

20   The two computations P7 line 7 refers to were done with the cloud/cloud distance tool of CloudCompare. The distances between the 129 GPS points and the ALS grid were computed with a local 2.5D Delaunay triangulation of the latter. Then, the vertical component was obtained whose statistical results were presented in Table 3. The, ALS – SfM comparison was done between the nearest points of the respective clouds.

This has been clarified in Section 3 of the manuscript.

25   P8 line 13. Please add a photo of your target. If you have a 12cm diameter circle in the centre, then how do you accurately place the GCP in Photoscan? Are you using some machine assisted algorithm? At 25m, the P4 camera will give you 1.3 cm pixels at nadir. This means that you target centre could be almots 10 pixels wide. How do you find the exact centre and so benefit fully from the accuracy of the RTK GPS? Note that errors at this stage, combined with your co-linear steup of GCPS could contribute greatly to rotational errors of the whole point cloud.

30   The centre of the targets was manually identified, without any machine assistance. The identification of the target centre relied on three concentric geometries, which were respectively used depending on the camera-GCP distance and the specific light conditions of each case. The smallest target was the CD inner circle with approximately 3.5 cm of diameter. This was used whenever visible. For the furthest targets and in those cases where the whole CD or

4

tile were reflecting too much light to the camera, the CD or tile centres were estimated based on the shape of their boundaries. Later, fast flipping through photo focusing on single GCP at a time (with the PageUp / PageDown keys in PhotoScan) helped to adjust the estimation of the target centre. This procedure turned consistent the location of the GCP among all camera views. Yet, this does not prevent introducing errors when identifying GCP target locations.

A photo of the target has been added to Figure 3, together with two more panels showing how a target is seen from the UAV paths 1 and 2. A new Section 5.3.3 clarifies the GCP identification procedure and the effects it has on accuracy.

P10 Figure 3. This is not a good view since scales are hard to determine. Better use a side view and a top view, both in orthometric perspectives so that a scale bar can be added.

Two scales were added in the perspective view of the DSM as references (for the corridor width and bank scarp height). Figure 3 has been expanded with two more panels showing an orthometric top view from Photoscan and an schematic side view with the UAV positions (since the sideview in Photoscan turned confusing with too many photographs).

Also, the choice of linear flight paths (here called tracks) parallel to the shore is again highly sub-optimal. This will only contribute to possible rotation errors. A grid pattern with multiple views would have been much more stable.

We have included a discussion on UAV paths in Section 5.3.2.

Figure 4. Please overlay the image footprints.

It has been done.

P11 From here you only use vertical error estimations to characterise method sucess. But as stated above, you could have other linear errors affecting the model. I note that the error distributions are bimodal with a dip for the number of errors in the 0 bin. This is consistent with a block rotation where few points (along the line of GCPs) are exactly corect. Many are either too high or too low. But this is not a vertical error in the photgrammetry process, it is the effect of rotation.

Thanks for this interesting observation. We have plotted the elevation errors at the rotational plane to analyse the signs and distances to the rotation axis. Indeed, this tendency is confirmed showing that errors at the floodplain and the terrace not only have respective positive and negative biases (as already presented in Table 2, column for Test 3), but also present a consistent trend across the rotational axis. This is then most likely caused by a small model rotation. We also acknowledge the role of vegetation cover (grass over the floodplain) as a source of overestimating ground elevations, and we do not discard non-linear effects on the terrace (beyond GCP limits), as possible errors present in the DSM that result in the achieved overall model accuracy. Overall, we agree with the analysis on the basis of the results, and do not discard the influence of other error sources that may contribute to enhance the linear trend.

> The analysis of linear rotation of the model is in a new section 4.3, and the results are discussed in section 5.1.

P13, Figure 7 Before you decide to crop data, you must show all the data. If you do crop, please select an objective criteria. e.g. 100 m buffer around each GCP. At the moment, the data looks manually cropped to variable distances away from the GCPs. A more rigorous approach is needed.

> The crop criterion along the floodplain had the intension to avoid the lines of brushes that lay across it (visible from the aerial photograph in the background). This shape was the result of cropping the LIDAR data prior to the comparison with the SfM point cloud.
>
> For a more robust approach, the ALS data has been cut along the boundaries of the SfM dense point cloud (visible in Figure 3), which are bounded by the area photographed from the nadiral UAV view (track 2). This criterion results in a overlapping domain between ALS and SfM data with an approximate constant width of 42m. Figure 7 now shows all available data.

Anonymous Referee #2:

The paper covers mapping a 1.2 km long river bank using a low-cost drone and structure from motion, and a comparison of this method with airborne laser scanning and RTK-GPS data. I do find this to be an interesting topic relevant for those working with morphology, environmental assessment and measurements in rivers, and it shows the potential of using drones and photogrammetry to gain data for river analysis. The comparison between different methods is also useful and relevant for other similar data collection efforts.

The paper is introduced in the abstract mostly as an example of developing a lowcost drone and the SfM method to measure the bank processes. The authors have employed a commercially available drone and commercial available software for this process, which in practice means that you already have a low-cost technique readily available. This is then applied here to a new problem, and I think the manuscript should be focused on what is new here from the many other applications of the same combination of drone/software.

Issues related to the SfM procedure is covered in detail in another comment, but in line with the previous comment I would also like to ask for some more discussion in the paper on: - The linear placement of the GCPs and the effect this might have on the point cloud. The placement of the control points and the effect this has on accuracy beyond the control points, and this could be combined to a more through discussion. - Issues related to the selection of flight paths only in parallel with the river bank that was measured.

> We thank the referee for his comments which helped improving the manuscript.
>
> A new section 5.3 has been added to discuss the novel challenges that the case study presents for the UAV-SfM application. A discussion on the linear placement of GCPs and its effect on the point cloud has been done in section 5.3.2. The placement of GCPs and their effect on the accuracy beyond GCPs has been discussed in sections 5.1 and

5.3.1. The main effect is the non-linear distortion beyond GCPs that produces the "dome" shape of the model, visible in Figure 7 at the extremes of the reach. The selection of parallel UAV paths and their role in the model registration has been discussed in the new section 5.3.2.

I also think it would be good to show the targets used to define the GCP (what was the size of the tile?), and maybe also a picture showing how these looked in the images from the drone and how they were identified in Photoscan since this is relevant for the accuracy.

A photo of a target has been added in Figure 3, together with two more panels that show how it is seen from UAV tracks 1 and 2.

The plaques were 40x40 cm (this has been added in section 3.2).

The targets were manually identified in Photoscan, and with the help of PageUp/PageDown keys we achieved consistency between all photos focusing on every target. This was useful since the target resolution varied with the sensor-GCP distance and some plaques at oblique perspectives reflected too much light to identify the CD (usually from track 1 and far away from the cross-section where the target was). In these cases, the background texture with the plaque boundaries were also used as references to locate the plaque's centre. If the plaque's centre was not clear enough to be identified, the GCP at that photo was discarded. The explanation and discussion of this criterion has been added to the new section 5.3.3.

Further on GCPs, on P12 there is a discussion on the GCP identification between tracks. It would be particularly interesting to see some more info on how well you think the accuracy of the GCP identification from pictures were for Track 1 were you see the GCP tiles at an angle in all pictures. To what extent do the identification of the tile centre influence the results.

Indeed, from the inclined angle of track 1 a smaller target area was captured, proportionally diminished by the cosine of the viewing angle with respect to the normal of the plane in which the GCP laid (say alfa). Following the previous explanation, this created more light reflection especially from the largest distances (oblique in two directions), but logically there also was a lower resolution to identify the target centres. The error introduced by a coarser resolution translated into elevation errors, and these directly affect rotational errors. On the other hand, the lateral view helped to compensate for this, since this elevation errors decreased with the cosine of alfa. Yet, positioning errors in transverse direction are relevant to quantify bank erosion rates, so these should be kept as low as possible, for instance, with inclined targets.

A clarification on the influence of GCP identification on accuracy and a recommendation have been added in the new section 5.3.1.

P7 – Was the grid from the ALS automatically generated from the scanner software or did you make it from the 10 points pr. square meter measured by the instrument? If it was automatic, could generating a finer grid improve the ALS results?

We did not process the raw data because we did not have access to it. We only worked with the 0.5x0.5m grid provided to us. The grid resolution is in principle limited by the footprint size of the laser beam on the ground and

the number of points per square metre. The footprint size was approximately 0.16m (one third of the grid resolution), from the beam divergence angle and the flight height. So, a finer grid could have been produced, for instance a 0.33x0.33 m grid from the 10 points/m² to approximately have one cell per each point. In this sense, the ALS results could have probably improved to capture more irregularities on the ground, which for banks proved essential. Still, even with a finer resolution, ALS can only survey 2.5D without capturing undermined profiles. These clarifications were added to sections 3 and 5.2.

P8 – Did you use automatic or manual settings for shutter speed, ISO, etc.?

We used automatic camera settings. Some considerations on this respect have been added in section 5.3.3.

P10 – Figure 3: A top-view perspective could be added to improve the understanding of camera positions.

A top view has been added to Figure 3, with two lines representing UAV paths 1 and 2-4.

P10 – Line11: How was the removal of trees etc. done?

The removal of vegetation from the point cloud was manually done in PhotoScan, simply by rotating the DSM and selecting those points above the surrounding ground level. Trees were easy to remove and some bushes required finding a correct perspective not to erase points from the ground.

P11 – Table 2: Can you give a short explanation for the colour scale in the caption? Do the colour change for every 0.01 meters? I also think grouping mean and std.dev. together like it is done for the "all grounds" would be more readable also for Grassland, Bank and Terrace.

For the mean values, the colour scale highlights the deviation from the zero value. For the naked eye it is possible to distinguish colour changes every 0.005 m, for the given range of values between -0.13 and +0.13 m (Table 2). In the case of the standard deviation, the colour scale highlights the deviation from the zero value too, but for a range of values between 0.00 and 0.13 m. Table 2 has been rearranged according to the suggestion and a description of the colour scale has been added in the caption.

P13 – Figure 7 is hard to read. Is it possible to divide it into a panel with different sections of the bank in each panel to improve the readability of the figure?

Figure 7 has been divided into two panels to increase the data visibility.

P13 – Figure 8. I assume this is based on results after the removal of the data outside the GCP limit. How is the GCP limit defined?

That is correct. The limit was defined by cross-sectional straight lines at the centre of the extreme GCPs. These lines have been added to Figure 7.

P16 Figure 10a: Do I understand it correctly that the change of elevation of the flood plain is mainly caused by development of the grass?

That is correct. The floodplain grass is mowed every year in October and usually grows during spring and summer time. The development of grass can be now observed in a new Figure 13 showing UAV photos from track 1.

P16: Figure 10. Would it be possible to illustrate the development here by also showing the images of at least some of the observations? The data presented in figure 10 is useful, but since there is both images and DTMs it would be interesting to see these processes and the basis for the development of figure 10.

A new Figure 13 has been added to show the development through three consecutive surveys at km. 153.9 (cross section 4), with a short description of processes linked to Figure 10 (called Fig. 12 in the new manuscript).

P17-line 29: Can0t you just write "A RMSE of 2.8 cm"?

Of course, thanks.

P18 – Line19: Do you think GCP0s at the bank toe would reduce the error? With reference to the previous comment on GCP placement and the further discussion on page 18, what was the rationale for the selected choice of GCP locations?

We think that non-linear errors could be reduced if GCPs were placed at the bank toe, but at the same time, there was no clear evidence of this type of error at the bank face. Regarding linear errors, the contribution to avoid or reduce rotation errors around the GCP axis would be minor, especially compared to wider horizontal GCP distributions across the floodplain. This is because the bank was roughly 3.5 metres high and its horizontal extent was also relatively short, compared to the floodplain that could allow for much larger cross-sectional distances to stabilize the DSM. What is more, GCPs were not systematically placed at the bank toe throughout the surveys for practical reasons. First, it was faster just to place GCPs on the floodplain than to descend to the bank toe, measure the coordinates, climb up, fly the UAV and sometimes recover the plaques afterwards (not all of them were left on the field to save them from vandalism). Second, we tried placing plaques at the bank toe but ship waves were able to take them away.

Therefore, the GCPs were located only over the floodplain, following the bankline. With sufficient cross-sectional GCP footprint and photo overlaps, the model should be stable enough to measure bank erosion, as in the case study presented. The criterion has been indicated in section 3.2, and a discussed in section 5.3.2.

A last question just out of curiosity. Was the flight done in autonomous mode or under control? What regulations govern the use of small drones for research purposes in this area? I understand that this varies between countries and could be an issue in planning similar st

The flight was done in autonomous mode with the software UgCS. There are regulations regarding no-fly zones that are typically close to airports (see https://kadata.kadaster.nl/dronekaart/) and pilot licenses are now necessary to fly UAVs. It is true that it can be an issue to fly UAVs so it is necessary to check beforehand what the local regulations are and sometimes ask for specific permissions before a mission.

A low-cost technique to measure bank erosion processes along middle-size river reaches

Gonzalo Duró[1], Alessandra Crosato[1,2], Maarten G. Kleinhans[3], Wim S. J. Uijttewaal[1]

[1] Department of Hydraulic Engineering, Delft University of Technology, PO Box 5048, 2600 GA Delft, the Netherlands
[2] Department of Water Engineering, IHE-Delft, PO Box 3015, 2601 DA Delft, the Netherlands
[3] Department of Physical Geography, Utrecht University, PO Box 80115, 3508 TC Utrecht, the Netherlands

Correspondence to: Gonzalo Duró (G.Duro@tudelft.nl)

~~Diverse methods are currently available to measure river bank erosion at broad-ranging temporal and spatial scales. Yet, no technique provides low-cost and high resolution to survey small-scale bank processes along a river reach.~~ We investigate the capabilities of Structure-from-Motion (SfM) photogrammetry applied with imagery from an Unmanned Aerial Vehicle (UAV) to measure bank erosion processes ~~describe the evolution of riverbank profiles~~ in middle-size rivers. This technique offers a unique set of characteristics compared to previously used methods to monitor banks, such as high resolution, low-cost and relatively fast deployment in the field. We analyse a 1.2 km restored bank of the Meuse River with complex vertical scarps laying on a straight reach, features that present specific challenges to the UAV-SfM application. ~~The bank erosion cycle is used as a reference to assess the applicability of different techniques.~~ We surveyed ~~1.2 km of a restored bank of the Meuse River~~ eight times within a year, combining different photograph perspectives and overlaps to identify an ~~efficient~~ effective UAV flight ~~to monitor banks~~. The accuracy of the Digital Surface Models (DSMs) was evaluated ~~compared~~ with RTK GPS points and an Airborne Laser Scanning (ALS) of the whole reach. An oblique perspective with eight photo overlaps and 20 m of cross-sectional ground-control point (GCP) distribution were ~~was~~ sufficient to achieve the ~~highest~~ relative precision to observation distance of ~1:1400 and ~~, with~~ ~~10~~ 3 cm RMSE, complying with the required accuracy ~~error range~~. A complementary nadiral view increased coverage behind bank toe vegetation. ~~The DSM and ALS had comparable accuracies except on banks, where the latter overestimates elevations.~~ The GCP footprint across the floodplain proved critical to avoid rotation of straight elongated domains, so improvements to the adopted approach are recommended. Sequential DSMs captured signatures of the erosion cycle such as mass failures, slump-block deposition, and bank undermining. Although this technique requires low water levels and banks without dense vegetation as many others, it is an inexpensive and fast-in-the-field alternative ~~is a low-cost method~~ to survey reach-scale riverbanks in sufficient resolution to quantify bank retreat and identify morphological features of the bank failure and erosion processes.

1 Introduction

Bank erosion is a fundamental process in morphologically active river systems, and much research has been devoted to understanding, quantifying and modelling it from disciplines such as engineering, geomorphology, geology and ecology. River bank erosion involves interconnected physical, chemical and biological processes (e.g., Hooke, 1979; ASCE, 1998; Rinaldi and Darby, 2008), resulting in a complex phenomenon that is difficult to thoroughly understand and predict (e.g., Siviglia and Crosato, 2016). Predicting and monitoring bank erosion is necessary for sound river management strategies and also important for both socio-economic problems, such as preventing material losses (e.g., Nardi et al., 2013), and environmental challenges, for instance, promoting habitat diversity through river restoration (e.g., Florsheim et al., 2008) and improving water quality (e.g., Reneau et al., 2004).

Bank erosion can be monitored with different spatial resolutions, time frequencies and accuracies. The techniques that identify the temporal change in vertical bank profiles detect and quantify the different phases of the erosion cycle (Thorne and Tovey, 1981). This characteristic helps distinguishing the factors influencing bank erosion and their relative role in the whole process (e.g., Henshaw et al., 2013). On the other hand, a simple record of sequential mass failure events (see Fukuoka, 1994, for a graph of failure-driven retreat) is sufficient to track rates of local bankline retreat and estimate eroded volumes, but does not provide further information on the role of single factors governing the bank erosion process. In navigable rivers, for instance, it is important to differentiate the effects of vessel-induced waves from the effects of river flow, as well as those of high flows and water level fluctuations. This requires high spatial resolution and relatively frequent measurements that usually involve expensive equipment and field logistics when monitoring large extensions. In this context, Structure from Motion (SfM) photogrammetry appears a promising low-cost Still no proven low cost technique is to capable of measuringe bank erosion processes along extensive distances (Fonstad et al., 2013).

We investigate whether the resolution, precision and frequency of acquisition of Structure from Motion (SfM) photogrammetry applied with imagery from a low-cost multi-rotor Unmanned Aerial Vehicle (UAV) is capable of monitoring banks at the process scale along a middle-size river reach. In order to do that, we compare the SfM-based Digital Surface Model (DSM) with Real-Time Kinematic (RTK) GPS measurements and Airborne Laser Scanning (ALS), and analyse erosion features in bank profiles considering the erosion cycle as a reference to distinguish approaches that measure bank erosion. The case study site is a 1.2 km straight river reach with reach of the Meuse River near the city of Gennep, the Netherlands, which has recently undergone a large bank restoration project . complex vertical scarps. This type of linear domain with vertical surfaces represent challenges to the UAV-SfM application, since special UAV paths and camera angles may be needed to capture the bank area and rather aligned GCPs along banks may result in rotated solutions during the model linear transformation.
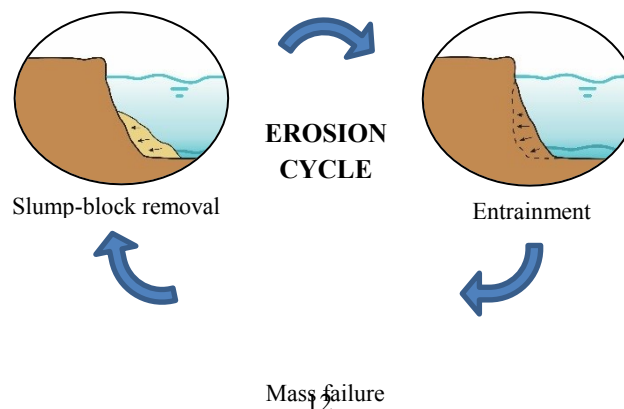
The study site is located in the Meuse River near the city of Gennep, the Netherlands, which has recently undergone a large bank-restoration project. The Meuse is a heavily regulated river used as navigation route to connect the eastern part of Belgium and the Netherlands to the industrial area in the West and the port of Rotterdam. The restoration aims to re-naturalize the previously protected banks, which are now allowed to erode. Here we take advantage of knowledge of the

5   original bank and of a rare event of extremely low water level.

2 Framework of analysis

2.1 Bank erosion cycle

Bank erosion may consist of three phases (Thorne and Tovey, 1981): fluvial entrainment of near-bank river-bed and bank material, mass failure, and disintegration and removal of slump blocks. These three phases are particularly important for

10   cohesive banks since their retreat is typically delayed by the protection offered by slump blocks at their toe (Thorne, 1982; Lawler, 1992; Parker et al., 2011). The waste material settles at the bank toe where it remains for a time depending on its resistance to fluvial erosion and on the flow capacity to transport the blocks. In contrast, loose waste material from non-cohesive banks is generally transported away relatively quicker by the river flow, leaving the bank sooner unprotected. Entrainment of near-bank bed material and the intact bank face occurs once the bank toe is exposed again (e.g., see Clark

15   and Wynn, 2007), which continues until the collapse of the upper bank. Mass failure occurs due to geotechnical instability, which can be triggered by different factors, such as fluvial bank-toe erosion (e.g., Darby et al., 2007) or a rapid drawdown of the river stage (e.g., Thorne and Tovey, 1981; Rinaldi et al., 2004).

Not only the river flow triggers the bank erosion cycle but other drivers can contribute to it as well. For instance, subaerial processes may weaken the bank and accelerate later fluvial erosion (Lawler, 1992; Kimiaghalam et al., 2015) or

20   also act as direct agent of erosion (Couper and Maddock, 2001). These effects are included in the entrainment phase for the former example and in the mass failure phase for the latter, which respectively promote entrainment or deliver material to the bank toe. Figure 1 illustrates the three phases of erosion in schematic cohesive banks. This representation shows a homogeneous soil which undergoes a continuous cycle of erosion with varying water levels.
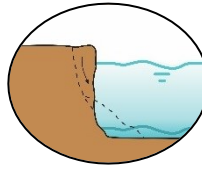
25

EROSION CYCLE

Slump-block removal

Entrainment

Mass failure

Figure 1: Schematic bank erosion phases: Slump-block removal (left), entrainment of bare bank (right) and incipient mass failure (centre)

Bank erosion can be analysed and measured at two different scales, i.e., the fluvial process and the river cross
5 section. The measurement at the process scale considers the bank face disintegration over time with evidence of erosion phases (Fig. 1): the mechanisms of erosion develop and are captured at the vertical dimension of the bank. The measurement of bank erosion at the cross-sectional scale, which can be referred to as bankline retreat, consists of tracking banklines over time. In this case, the focus is on the planimetric changes of the bank edge and estimations of eroded volumes and sediment yield. The former approach deals with processes and mechanisms (e.g., Rinaldi and Darby, 2008), whereas the latter with
10 landscape development at larger spatial and temporal scales. Bank-erosion studies determine the survey method based on their aims and scales of interest, whereas in turn a given methodology constraints the scope of the findings (Massey, 2001; Couper, 2004). Thus, it is important to identify capabilities and limitations of each survey technique in the context of river banks, which are inherently steep features with small-scale irregularities independent of the scale of the river.

2.2 Techniques to measure bank erosion

15 Measuring techniques have four essential characteristics: the extent, resolution, precision and frequency of measurements. Extent refers to the area or distance along the river covered by each survey; resolution indicates the distance between surveyed points; precision is the accuracy of position of each surveyed point; and frequency derives from the time interval between consecutive surveys of the same spatial extent or point. The scale of interest may vary among disciplines (e.g., geomorphology, engineering, ecology), so that a diversity of techniques is available with varying spatio-temporal
20 windows of inquiry (Lawler, 1993). Even though the methods currently adopted to measure river bank erosion range from photo-electric erosion pins to terrestrial laser scanning, they have high resolution in either time or space (Couper, 2004; Rinaldi and Darby, 2008).

The methods to determine bankline retreat and to estimate eroded volumes are typical of remote sensing, for instance, ALS and aerial photography. The former technique has typical resolutions of 1 and 0.5 metres, and covers up to
25 hundreds of square kilometres per day. Bailly et al., (2012) indicate decimetre vertical precision, which depends on several factors including beam footprint size, aircraft inertial measuring system, on-board GPS, vegetation cover and filtering technique. ALS has been successfully applied to identify river morphological features, such as bar tops (Charlton et al., 2003) and riffle–pool and step–pool sequences (Cavalli et al., 2008). In addition, sequential ALSs were used to quantify volumes of eroded banks to subsequently estimate pollutant loads, achieving reasonable results for those aims (Thoma et al.,

2005). However, banks are particularly steep areas where this technique tends to increase the elevation uncertainty (Bangen et al., 2014). Therefore banks are regions where lower ALS accuracies are expected compared to horizontal and flat areas.

Aerial photography has also been applied to measure bank migration, which is a useful source of information, especially if historical imagery is available over extended periods of time. Yet, it provides only limited information on bank heights. Thus, this planform survey technique requires other methods to estimate eroded volumes. For example, photogrammetry can serve to quantify volumetric changes from overlapping photographs (Lane et al., 2010); or ALS may provide recent topographic elevations to reconstruct past morphologies (Rhoades et al., 2009). Bank retreat can also be estimated through other approaches, such as those described by Lawler (1993), that include planimetric resurveys for intermediate timescales (years) and sedimentological and botanical evidence for long timescales (centuries to millennia).

Measuring bank erosion at the process scale involves measuring the evolution of the vertical bank profile over time and several techniques are currently available to that end. Traditional methods include erosion pins and repeated cross-profiling, which provide two-dimensional information with resolutions that respectively depend on the number of pins and points across the profile (Lawler, 1993). Erosion pins are simple and effective, but their accuracy may be affected by several factors, such as subaerial processes (Couper et al., 2002). More advanced versions are the photo-electric erosion pins that automatically track the bank face during different erosion phases (Lawler, 2005). Cross-profiling can be done with GPS or total stations with point accuracies of a few centimetres or millimetres, yet with spatial and temporal resolutions that may not be sensitive to very localized or intermittent erosion (e.g., Brasington et al., 2000).

Bank geometries can currently be surveyed with their three-dimensional complexity through a number of techniques whose geomorphic applications are broader than bank erosion studies: terrestrial photogrammetry, Terrestrial Laser Scanning (TLS), boat-based laser scanning and SfM photogrammetry. Terrestrial photogrammetry has shown detailed bank representations, with approximate resolutions of 2 cm and precision within 3 cm, covering up to 60 metres of banks (Barker et al., 1997; Pyle et al., 1997). Yet, this method can be labour-intensive and requires an accessible bank (Bird et al., 2010), known camera positions and sensor characteristics, ground-control points, among other considerations (Lane, 2000). TLS has shown detailed erosion patterns from sequential surveys, with millimetre resolutions, which in practice are usually reduced to 2–5 centimetres, and approximate final accuracies of 2 cm (Resop and Hession, 2010; Leyland et al., 2015). O'Neal and Pizzuto (2011) proved the advantages of 3D TLS in capturing patterns (e.g., overhanging blocks) and quantifying eroded volumes over 2D cross-profiling. Even though TLS could cover thousands of meters, in practice the extents are generally smaller due to accuracy decrease, large incidence angles, occlusion, etc. (Telling et al., 2017), so several scans are necessary to measure long distances. For instance, Brasington et al. (2012) surveyed a 1 km river reach scanning every 200 m along the channel. An alternative boat-based laser scanning can continually survey banks with comparable resolutions and accuracies to those of TLS, with great time reduction but involving other field logistics, resources and post-processing (Alho et al., 2009).

SfM photogrammetry has been applied to measure banks to show its potential use as survey technique with different sensors and processing systems (Micheletti et al., 2015; Prosdocimi et al., 2015). Micheletti et al. (2015) indicated root mean

square errors (RMSE) within 7 cm, when combining a 5MP smartphone or a 16MP reflex camera with either PhotoModeler or 123D Catch processing systems. Prosdocimi et al. (2015) identified eroded areas of a collapsed riverbank and computed eroded and deposited volumes with a precision comparable to that of TLS. Bangen et al., (2014) matched the resolution and practical extent of this technique to those of TLS, when SfM photogrammetry is used to survey river topography through aerial platforms (e.g., Fonstad et al., 2013). The relatively recent and fast development of UAV technology to take airborne photographs has greatly expanded the applications of SfM photogrammetry (Eltner et al., 2016). Recently, SfM has been applied to quantify bank retreat at streams and small rivers with a fixed-wing UAV along several kilometres with 12 cm resolution (Hamshaw et al., 2017). This study showed the UAV-SfM capabilities to produce extensive 2.5D DSM from a 100 m high nadiral view, which achieved 0.11 m mean error and 0.33 m RMSE compared to TLS. However, this work generated DSMs similar to those of ALS, which allow for volume computations and bankline retreat, but did not use the full 3D capacities to investigate undermined banks or identify erosion processes.

Applications of this combined technology span in scale and complexity, covering glacial dynamics (Immerzeel et al., 2014), landslides (Turner et al., 2015), agricultural watersheds (Ouédraogo et al., 2014), fluvial topography (Woodget et al., 2015), etc. The accuracy achieved relative to the camera-object distance for the mentioned diverse settings was approximately 1:1000, with distances ranging from 26 to 300 m and different cameras, lighting conditions and surface types. Interestingly, this precision was also found for terrestrial SfM photogrammetry at different scales by James and Robson (2012). However, other experiences showed lower accuracies, e.g., ~1:200 for moraine-mound topography (Tonkin et al., 2014), and on the other hand higher ones, such as ~1:2100 for fluvial changes after a flood event (Tamminga et al., 2015). Although it is not possible to generalize a precision for all settings, ~1:1000 seems an encouraging reference (RMSE of 10 cm for 100 m camera-object distance) to consider for unexplored conditions.

Every combination of field site, camera sensor, ground control points (GCPs) and SfM package in principle requires different photo overlaps, resolutions and perspectives (image network geometry) to achieve certain model accuracy and resolution through UAV-SfM (Elter et al., 2016). This is caused by different surface textures (Cook, 2017), lighting conditions (Gómez-Gutiérrez et al., 2014b), camera characteristics (Prosdocimi et al., 2015), GCP characteristics (Harwin and Lucieer, 2012), and SfM algorithms (Eltner and Schneider, 2015). Knowledge to improve the quality of SfM digital surface models keeps expanding by investigating isolated variables, for example, assessing the influences of number and distribution of GCPs (Clapuyt et al., 2016; James et al., 2017) or optimizing camera calibration procedures to manage without GCPs (Carbonneau and Dietrich, 2017). The flexibility, range, high resolution and accuracy that UAV-SfM proved in other conditions shows promising for analysing bank erosion processes throughout the scale of a middle-size river.

The monitoring of bank erosion processes in the case study herein has two specific challenges for the UAV-SfM technique. First, the bank has steep, vertical and undermined surfaces along the domain. Second, the target area is a straight reach with a large length-to-width ratio. The first aspect may require non-conventional UAV paths and camera angles to be able to adequately capture the bank area. The second matter introduces a challenge to georeference the model with rather aligned GCPs, which may result in false solutions rotated around the GCP axis during the model linear transformation. This

could be the case since GCPs are to be placed in the bank surroundings to be captured from the UAV, and this target area consist of an overall linear domain. Therefore, the GCP distribution and the image network geometry particularly have key roles in the UAV-SfM workflow applied to measure bank erosion at the process scale.

3 Methodology

We used the flexibility of a multi-rotor UAV platform to capture photographs from different perspectives of a 1200 m long riverbank and through SfM photogrammetry derived several DSMs over one year period. We describe the study location in Sect. 3.1, the UAV paths for photo acquisition in Sect. 3.2, and the SfM imagery processing in Sect. 3.3. In order to assess the capabilities of this survey methodology to measure bank erosion at the process scale we proceeded in ~~three~~ four steps. First, we verified the elevation precision against 129 RTK GPS points of several DSMs obtained with diverse number of photographs and camera orientations. In this way, we identified an effective number of images to acquire the bank topography with high accuracy. Second, we compared the chosen DSM with airborne LIDAR points to analyse elevation precision over the whole river reach, differentiating between areas of bare ground, grassland and banks. Third, we verified the georeferentiation accuracy regarding the model rotation around GCP axis. Fourth~~Third~~, we searched for bank features in SfM-based profiles and analogous ones from ALS, and for signatures of erosion processes along sequential SfM surveys.

For the first step, the analysis of the minimum number of photographs needed to achieve the highest DSM precision, we compared the DSMs with RTK GPS measurements to quantify vertical accuracy. We took 129 points across eight profiles on 18-01-2017 (see Fig. 4) with a Leica GS14 RTK GPS, whose root mean square precisions according to the manufacturer specifications are 8 mm + 0.5 ppm in horizontal and 15 mm + 0.5 ppm in vertical directions. On the same date, we flew the UAV along the bank four times with different camera angles and perspectives. Eight photograph combinations were considered to derive 8 DSMs. Then, the comparisons were done with the elevation differences between the GPS points and the corresponding closest ones of the DSM point clouds (e.g., Westoby et al, 2012; Micheletti et al., 2015). We used CloudCompare software (Girardeau-Montaut, 2017) for these computations.

In the second step, we compared the selected DSM from the previous analysis with a reach-scale survey technique, ALS, to analyse ~~elevation~~ topographic differences over the whole river reach. The ALS was carried out on 17-01-2017 from an airplane at 300 meters above the ground level. The laser scanner, a *Riegl LMS-Q680i,* measured a minimum of 10 points per square metre with an effective pulse rate of 266 kHz. We did not have access to the raw data and used the automatically generated ~~a~~ 0.5 m grid. We tested the ALS elevation precision against the 129 RTK GPS points using the vertical component of the closest distance to a local Delaunay triangulation of the ALS grid, due to the different resolutions between both datasets. Then, we comput~~ed~~ared the distances between ~~elevation of~~ the ALS grid points ~~with~~ and the corresponding nearest ones of the DSM point cloud. We did both computations with the standard cloud/cloud distance tool of CloudCompare, distinguishing between surfaces of grassland, bare ground and bank.

Third, we analysed the DSM spatial stability with respect to the potential axis of rotation around the GCPs, which in the case study laid over a narrow, elongated and straight domain. The GCPs distributed over the floodplain along the near-bank area defined the linear transformation from an arbitrarily scaled coordinate system to the real-world coordinates. In order to verify that the DSM was stable and the tendency to rotate around co-linear solutions did not affect the accuracy beyond the survey target, we computed a regression line with the GCPs to identify the potential axis of rotation for the DSM domain. Then, we projected onto the perpendicular rotational plane the DSM elevation errors corresponding to the GPS points and computed a second regression line to evaluate if there was a linear tendency that indicated a model rotation.

ThirdFourth, we made profiles across six sections of dissimilar erosion rates to contrast the bank representations of i) the SfM DSM, ii) the triangulated ALS grid, and iii) the RTK GPS points. The profiles were computed with MATLAB using i) the Geometry Processing Toolbox (Jacobson et al., 2017) adapted to slice triangle meshes, ii) a linear interpolation across the triangulated ALS grid, and iii) a projection of the RTK GPS points onto the exact cross-section locations. Then, we identified and analysed a cross section over which sequential SfM-UAV surveys showed different stages of the erosion cycle, since the bank erosion cycle was used as a reference to distinguish between techniques capable of measuring at either the process or the cross-sectional scale.

3.1 Study site

The study site is a restored reach of the Meuse River, which used to be a single-thread freely meandering river. The river was canalized to a straight reach of 120 m width, the banks were protected and the water levels regulated to improve navigability. However, several kilometres of banks have been recently restored through the removal of revetments and groynes, following the EU Water Framework Directive 2000/60/EC (http://data.europa.eu/eli/dir/2000/60/oj). This reactivated erosion processes to improve the natural value of the river. Important questions have then arisen regarding bank retreat rates and the new equilibrium of the river width. Monitoring bank evolution is necessary to answer these questions and to identify the need, if so, to intervene and at which locations.

The study site is the left bank of a 1200 m long straight reach (Fig. 2) located between the Sambeek and Grave weirs in southeast Netherlands. Seven years after restoration, this reach presents different bank retreat patterns, with sub-reaches of rather uniform erosion and others with embayments of different lengths. Grassy fields used for grazing cover the riparian zone, followed by crop fields across the floodplain. In the near-bank area there are poplar trees every 100 m, some of which have been dislodged during the erosion progression, which is possible to appreciate in Fig. 2 (left) considering the ~200 m embayment between the foreground tree and the next in the background.

17

Figure 2: Restored bank in the Meuse River, upstream view of first 300 m (left) and downstream view of middle 500 m (right). Bank erosion has caused a series of bays in the 1,200 meter restored reach. Note eroded bank sediment in suspension.

The study site was surveyed eight times with ~~a~~ the UAV in 2017. An extraordinary low water level in January provided the opportunity to compare the SfM photogrammetry with ALS and RTK GPS not only for the banks and floodplain, but also for the sub-aqueous terrace at the bank toe (see schematic cross sections in Fig. 2). This terrace was composed of bare soil, without vegetation or obstructions, which adds an extra surface for the comparative analysis. This extraordinary exposure was the consequence of a ship accident against the downstream weir of Grave (on 30 December 2016).

3.2 UAV flights for image acquisition

We used the low-cost UAV DJI Phantom 4 to take images of the banks. It has a built-in camera with a 1/2.3" 12 megapixels sensor and a 94° horizontal angle of view. Prior to the image acquisition, a network of Ground-Control Points (GCPs) was distributed ~~every approximately 50 metres~~ on the floodplain to georeference the DSMs (see Fig. 4). The GCP were spaced every approximately 50 metres along the reach, roughly following the tortuous bankline and avoiding proximity to trees, to simplify the field work and facilitate the GCP visibility from the UAV paths (see Fig. 3-4). This approach missed GCP locations at different elevations, as for instance at the bank toe, and relied on the cross-sectional GCP distribution for the stability of the DSM georeferentiation (see Sect. 3.3). The GCPs were 40 by 40 cm black ceramic tiles (Fig. 3c) fixed to the ground with a circular reflector (12 cm CD) at its centre for their fast recognition in the photographs (Fig. 3d-e show how a GCP is seen from tracks 1 and 2). We measured the GCP coordinates using the Leica GS14 RTK GPS unit, which was also deployed for the cross-profiling.

An initial flight plan was designed to photograph the banks from four different perspectives, to later compare the results of diverse combinations and find a convenient photo set to survey the target topography in subsequent campaigns. The UAV flew four times in straight parallel lines along the banks (Fig~~.~~. 3a,b,f) to simplify the set-up and save flying time, compared to paths that follow changes in bankline or include paths across the domain. The first track took oblique photos from above the river at a height of 25 metres and an average (oblique) distance to the bank of 40 metres (~25 m from the least retreated bankline). The second track had a top view from 40 metres above the floodplain level along the tree line (Fig.

18

. 2–4). The third and fourth tracks followed the same path as the second one in respective upstream and downstream directions, but the camera angle was 50 degrees forward inclined from the horizontal plane (see photo footprints in Fig. 4). These perspectives were thought to capture the tortuous and complex bank surface (Fig. 2, and 3a and 4), including undermined upstream- and downstream-facing scarps, with an average ground resolution of 2.1 cm per pixel. We considered a minimum resolution and accuracy of 1/25 times the bank height of the river as a requirement to detect erosion processes, which resulted in a maximum acceptable accuracy of 14 cm for the maximum bank height of 3.5 m at the case study.

We tested five specific combinations of photographs from the different UAV tracks. *Test 1* corresponds to the photo set of the first track only, which has the side view with the optimal coverage of the bank. *Test 2* stands for the nadir view alone, which is similar to the viewpoint of classic aerial photography. *Test 3* is a combination of the previous two sets. *Test 4* combines tracks 3 and 4, i.e. both paths from above the bank with the oblique forward perspectives in upstream and downstream direction, which allows views on all parts of the irregular banks. Finally, *test 5* utilizes the four tracks with all photographs (Table 1).

We also used the first oblique track to evaluate the minimum longitudinal photo overlap to efficiently capture the bank relief. The photo overlap along the river is a function of the UAV speed and distance to the bank, for a given maximum photo sampling frequency, which in the case of the deployed UAV is one every 2 seconds. Then, flying at 2 m/s along track 1 resulted in 20 photo overlaps for the most retreated areas and 16 for those zones with least bank retreat. Afterwards in the processing phase, we successively selected a decreasing number of overlaps by twos that resulted in four DSMs. These were *test 1a* when using all photos from track 1 (which is the same set as the aforementioned test 1), *test 1b* when using half of them, and so forth for *test 1c* and *test 1d* (see Table 1).

Table 1. Number of photographs and overlaps for the tests

	Test 1a	Test 1b	Test 1c	Test 1d	Test 2	Test 3	Test 4	Test 5
Track 1	293	147	73	37		147		293
Track 2					232	232		232
Track 3							232	232
Track 4							232	232
Min. overlaps	16	8	4	2	7	15	26	49
Max. overlaps	20	10	5	2	7	17	26	53

3.3 SfM ~~imagery processing~~workflow

The principles of SfM photogrammetry are similar to those of digital photogrammetry, but the former does not need specifications on camera positions and lens characteristics to reconstruct 3D structures. The camera extrinsic and intrinsic parameters are automatically estimated via tracking and matching pre-defined features in overlapping photos and an iterative bundle adjustment procedure, which results in a sparse point cloud (Hartley and Zisserman, 2003; Snavely et al., 2008; Westoby et al., 2012). Afterwards, the (dense) point matching is done at pixel scale to generate a detailed point cloud of the scene that has the final survey resolution. The point cloud can then be georeferenced with GCPs, ~~which is necessary when monitoring bank erosion through sequential surveys~~or a~~.~~ Alternatively, ~~GCPs~~ these can be incorporated for the iterative bundle adjustment as additional matched points, during which the georeferentiation takes place.

The use of GCPs is necessary to reference the model to a geographical coordinate system, to compute erosion rates and processes through sequential surveys. The georeferentiation process involves the Helmert transformation of the point cloud through 7 parameters that adjust its scale, position and rotation in a linear and rigid way (Fonstad et al., 2013). The estimation of these parameters is done through a least-squares regression with the GCPs identified in the UAV images. The propagation of linear errors is thus given by the accuracy with which the GCPs were measured (in this study with the RTK GPS) and then identified in the photographs. Further in the SfM workflow, GCPs can be used to refine the camera parameters estimated during the bundle adjustment, to reduce the non-linear errors that the estimation of the camera parameters may induce (Carbonneau et al., 2017). Ideally, well distributed, precisely measured, and accurately identified GCPs avoid excessive linear and non-linear errors in the point cloud. Yet, a third type of error given by the automated image matching process cannot be prevented with GCPs. These are local and random errors and represent the classic concept of precision.

We used Agisoft PhotoScan software to process the imagery. For a successful photo alignment from different UAV tracks (Table 1), the camera yaw, pitch and roll recorded during the UAV flight were necessary inputs. For this step we used three GCPs along the reach, two at the extremes and one at the middle, all close to the bank and easily visible from tracks 1 and 2. These approximate orientations and a priori known ground points helped obtaining a consistent sparse point cloud of the bank along the entire reach. The resulting camera positions and orientations of the photo alignment are visible in Fig. 3a, evidencing the UAV tracks. This figure also shows the DSM textured with colours from the photographs, in which the green area on the left side with white patches corresponds to the floodplain partially covered with snow (see also Fig. 3d-f) and the right brownish area is the terrace at the bank toe, with snow remains as well.
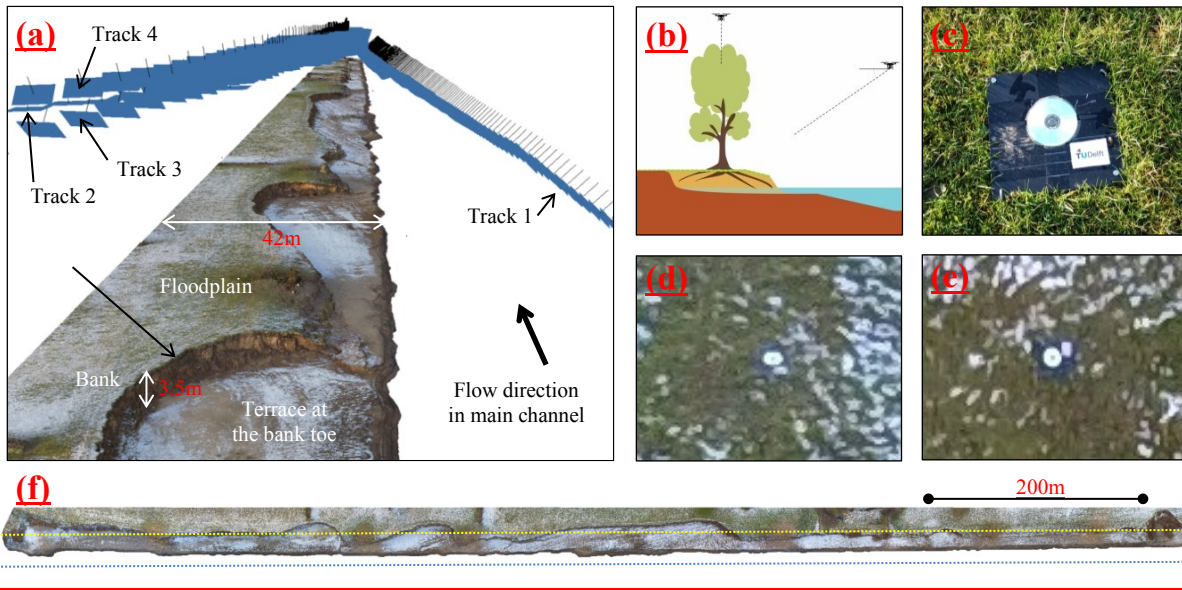
20

Figure 3: a) Camera positions and orientations in perspective view. The digital surface model shows the low-water condition during January 2017, which exposed a terrace at the bank toe. b) Cross-sectional scheme of UAV paths. c) Ceramic plaque with CD as ground control point on the floodplain. d) GCP in photograph from track 1. e) Same GCP from track 2. f) Top view of DSM with UAV track 1 in blue and tracks 2-4 in yellow.

After obtaining the sparse point cloud, we marked the remaining 15 GCPs (Fig. 4). Then, we refined the camera parameters by minimizing the sum of GCP reprojection and misalignment errors. This camera optimization adjusts the estimated point cloud by reducing non-linear deformations. Once the dense point cloud was computed, we removed the points outside the area of interest, as well as those points at the water surface, tree canopies and individual bushes at the floodplain. Finally, the point cloud was triangulated and interpolated to generate a triangle mesh. This mesh consisted of a non-monotonic surface that was later processed in MATLAB to plot 2D cross sections.
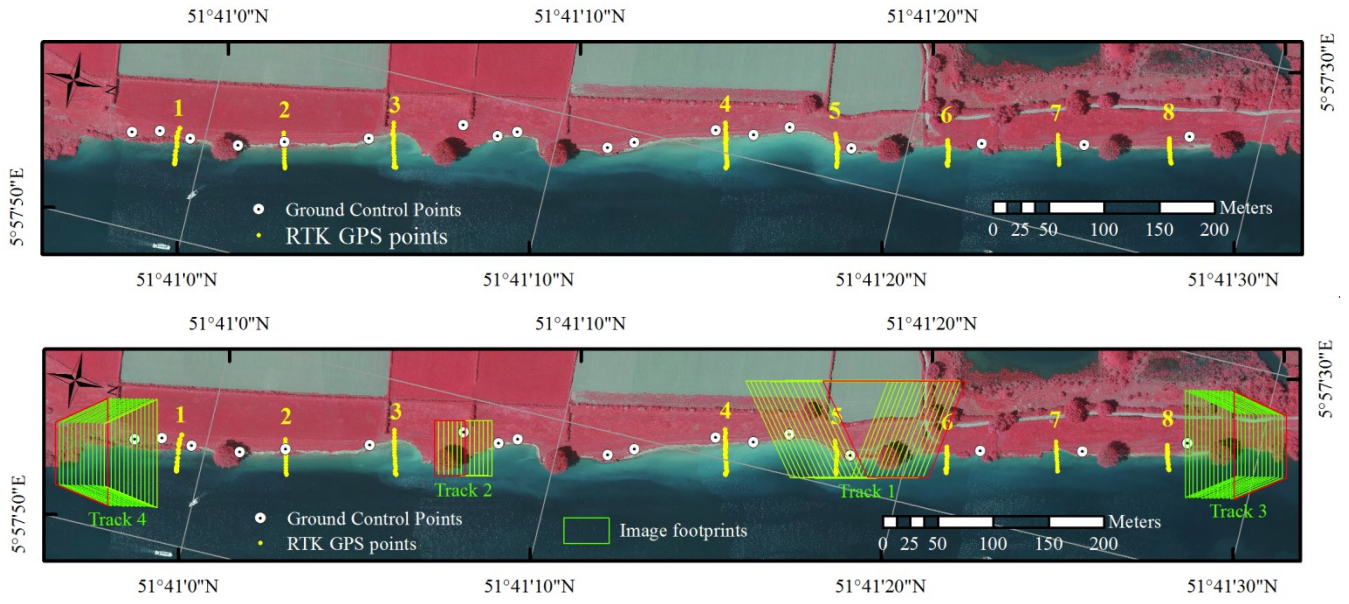
Figure 4: Study reach of the Meuse River with GCPs, RTK GPS measurements with and cross-section locations and numbers, and some image footprints for all UAV tracks.

4 Results

4.1 DSM precision: identifying necessary photographs

The sequentially decreasing photo overlaps of Track 1 (Table 1) produced four DSMs, tests *1a–1d*, whose elevation differences with the 129 RTK GPS points are presented in the histograms of Fig. 5. The elevation errors mostly ranged within 10 cm in all tests, but the mean and standard deviation (SD) presented some differences (Table 2 and dot with bar in Fig. 5). Tests *1a*, *1b* and *1c* presented mean values smaller than 1 cm and SD within 3–4 cm, while for test *1d* these values increased to 4 cm and 7 cm respectively (Table 2, rows 1–2). The mean errors on the bank area alone for test *1a*, *1b* and *1c* were lower than 1 cm (Table 2, row 45), but test *1c* had a higher SD of 7 cm compared to 4 and 3 cm of tests *1a* and *1b* respectively (Table 2, row 76). Then, tests *1a* and *1b* had the highest precisions and showed little error differences between them: less than 1 cm for all values in Table 2. Consequently, test *1b* with eight photo overlaps was as effective as test *1a* with 16 overlaps to achieve the highest DSM accuracy. In addition, test *1b* fully covered the tortuous bank area in contrast to test *1c*, especially at the perpendicular stretches of embayments (Fig. 3–4), which assured the choice of 8 image overlaps over 4, despite the general close performance of the latter in terms of accuracy (Table 2, all rows). Therefore, test *1b* became the reference for tests *1* and was used in combination with test *2* to generate test *3*.
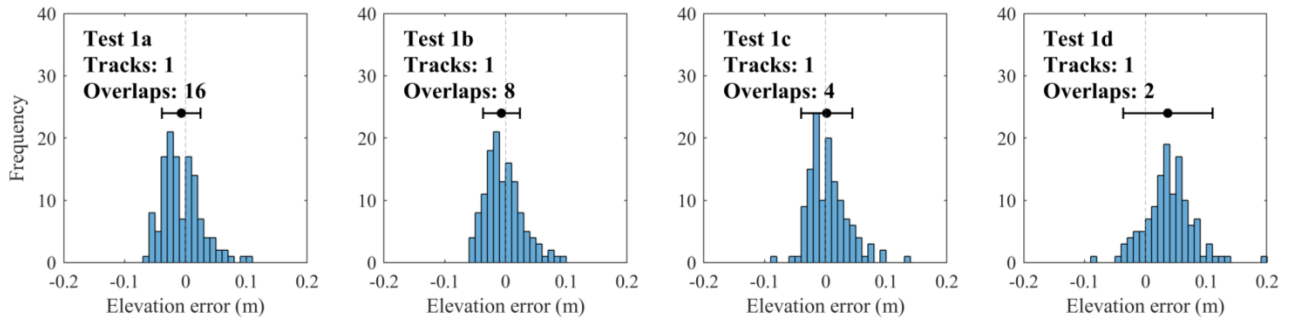
Figure 5: Elevation error distributions for SfM tests *1a*, *1b*, *1c*, and *1d*, assuming that the RTK points are correct and without error. Indicated overlaps are the minimum.
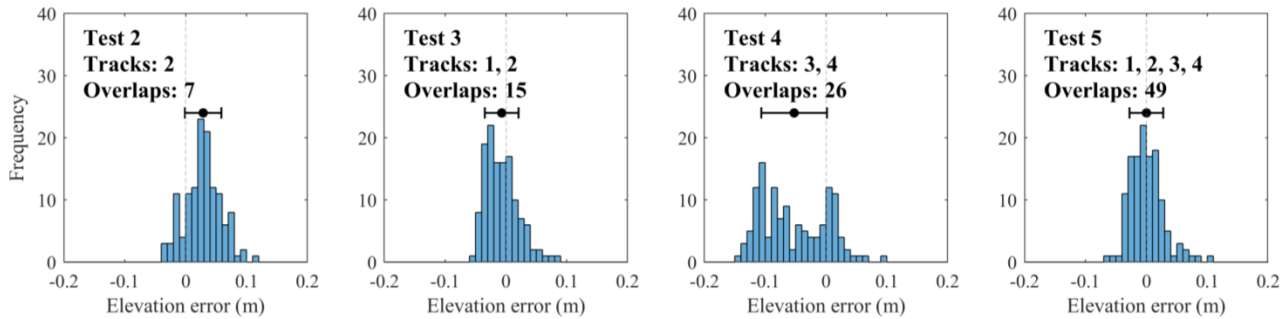
Table 2. Mean and standard deviation of elevation differences between SfM DSMs and GPS points. Colour intensity indicates the deviation from zero value with minimum/maximum of ±0.13 m.

~~Surface~~	~~Error (m)~~	~~Test 1a~~	~~Test 1b~~	~~Test 1c~~	~~Test 1d~~	~~Test 2~~	~~Test 3~~	~~Test 4~~	~~Test 5~~
~~All grounds~~	~~Mean~~	~~-0.01~~	~~0.00~~	~~0.00~~	~~0.04~~	~~0.03~~	~~-0.01~~	~~-0.05~~	~~0.00~~
~~-~~	~~Std. dev.~~	~~0.03~~	~~0.03~~	~~0.04~~	~~0.07~~	~~0.03~~	~~0.03~~	~~0.05~~	~~0.03~~
~~Grassland~~	~~Mean~~	~~0.02~~	~~0.01~~	~~0.01~~	~~0.02~~	~~0.02~~	~~0.01~~	~~0.01~~	~~0.02~~
~~Bank~~	~~-~~	~~0.00~~	~~0.01~~	~~-0.01~~	~~-0.01~~	~~0.05~~	~~0.01~~	~~-0.03~~	~~0.01~~
~~Terrace~~	~~-~~	~~-0.02~~	~~-0.02~~	~~0.00~~	~~0.06~~	~~0.03~~	~~-0.02~~	~~-0.09~~	~~-0.01~~
~~Grassland~~	~~Std. dev.~~	~~0.03~~	~~0.03~~	~~0.04~~	~~0.04~~	~~0.03~~	~~0.02~~	~~0.02~~	~~0.02~~
~~Bank~~	~~-~~	~~0.04~~	~~0.03~~	~~0.07~~	~~0.13~~	~~0.03~~	~~0.03~~	~~0.04~~	~~0.03~~
~~Terrace~~	~~-~~	~~0.02~~	~~0.03~~	~~0.03~~	~~0.06~~	~~0.03~~	~~0.02~~	~~0.03~~	~~0.02~~

Surface	Error (m)	Test 1a	Test 1b	Test 1c	Test 1d	Test 2	Test 3	Test 4	Test 5
All grounds	Mean	-0.01	0.00	0.00	0.04	0.03	-0.01	-0.05	0.00
-	Std. dev.	0.03	0.03	0.04	0.07	0.03	0.03	0.05	0.03
Grassland	Mean	0.02	0.01	0.01	0.02	0.02	0.01	0.01	0.02
-	Std. dev.	0.03	0.03	0.04	0.04	0.03	0.02	0.02	0.02
Bank	Mean	0.00	0.01	-0.01	-0.01	0.05	0.01	-0.03	0.01
-	Std. dev.	0.04	0.03	0.07	0.13	0.03	0.03	0.04	0.03
Terrace	Mean	-0.02	-0.02	0.00	0.06	0.03	-0.02	-0.09	-0.01
-	Std. dev.	0.02	0.03	0.03	0.06	0.03	0.02	0.03	0.02

Figure 6 shows the error distributions of the remaining four DSMs, i.e. tests *2–5*, which also were mostly within 10 cm, except for Test *4*. This test had evident higher errors than the rest, mostly concentrated at the terrace (Table 2, row ~~5~~7). Tests *3* and *5* had the lowest mean elevation errors, both lower than 1 cm, with the same SD at all surfaces that were lower than 3 cm. Test *2* presented a similar SD, but the mean was biased 3 cm. This test in combination with test *1b* slightly reduced the SD errors of the latter (Table 2, rows ~~5~~7 and ~~7~~6), but without significant overall improvements. All in all, tests

23

1b, *3* and *5* had the best performances with average errors lower than 1 cm and standard deviations within 3 cm, however with increasing number of photographs (Table 1). The most efficient one was then test *1b* that used the lowest number of photographs to achieve similar precision, especially on banks.

5   **Figure 6:** Elevation error distribution for tests 2, 3, 4, and 5. Ordinates indicate number of GPS points in each bin.

Interestingly, if we consider all tests, the elevation errors on grassland were similar to each other (Table 2, rows 3 and 6), means between 1 and 2 cm and SD between 2 and 4 cm, whereas the bank and terrace did not present this behaviour. Furthermore, while the bank values (Table 2, rows 4 and 7) did not correlate with those of all grounds (Table 2, rows 1–2), the terrace mean elevation differences (Table 2, row 5) linearly correlated with those of all grounds (Table 2, row 1) with R^2

10   = 0.97. Therefore, the error biases for all grounds throughout the tests were most likely due to the biases from the points over the terrace.

To conclude, despite virtually doubling the number of images in comparison with test 1b, the test *3* setup with a nadir track and a side-looking track was chosen for subsequent UAV surveys on the basis of two findings. First and most important, growing vegetation at the bank toe occluded parts of the target surface from the oblique camera perspective.

15   Second, the GCPs on the floodplain laid almost horizontal, which made them easier to identify from the top-view during an initial phase of GCP recognition in the photographs. Moreover, we found at later surveys that growing grass on the floodplain was sometimes blocking GCP plaques from the angle of vision of UAV track 1, for which using the nadir view of track 2 was advantageous to locate the plaque centres, preventing the otherwise disuse of some GCPs.

4.2 DSM precision over the reach: comparison with ALS

20   Compared to the ALS grid, test *3* point cloud showed a good agreement over most of the reach. This is observable from Fig. 7a, corresponding to the blue areas that indicate elevation differences lower than 5 cm. Yet, two notable regions surpassed this difference, notably the bank and the extremes of the reach. The latter were zones beyond the GCPs, where higher errors in the DSM are expected when using parallel image directions due to inaccurate correction of radial lens distortion (James and Robson, 2014; Smith et al., 2014). Consequently, the results outside the GCP limits cannot be

25   considered representative of the whole domain and they were discarded for the subsequent statistical comparisons (beyond the dashed lines in Fig. 7). Within the GCP bounds, the bank area presented relatively high elevation differences, which

makes the bankline visible in Fig. 7. Moreover, another sloped area at end of the terrace also presented higher differences than surrounding areas, which is visible as a thin light-blue line at bottom of the domain in Fig. 7a (see also Fig. 3a-b for other perspectives of this slope toward the channel bed).
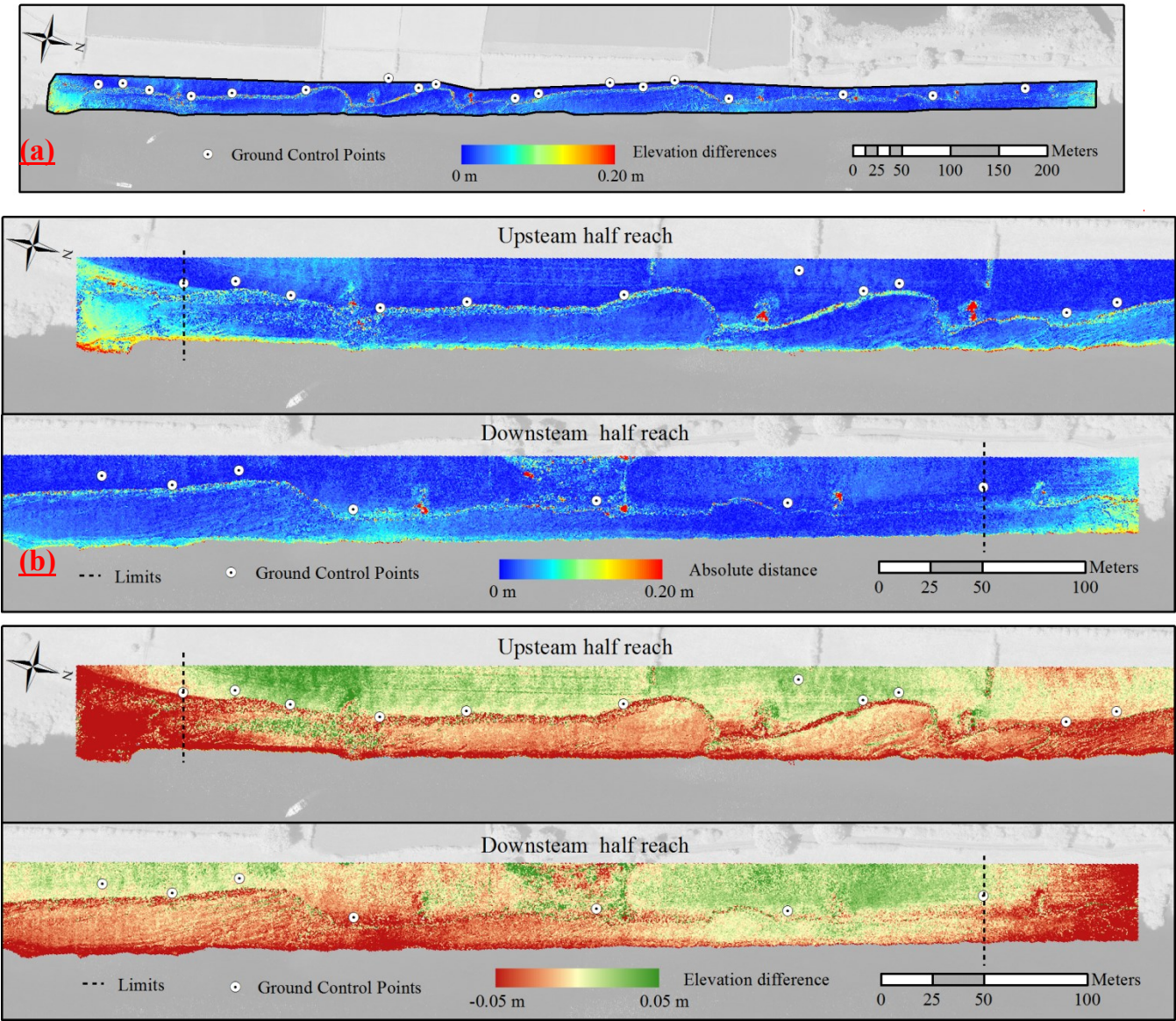

Figure 7: a) Absolute elevation differences between SfM and ALS along the reach. ~~Banks and areas beyond GCPs presented the highest differences.~~ b) Signed elevation differences between SfM and ALS with a smaller scale range.

Figure 7b presents signed elevation differences with a smaller scale range to highlight areas with positive and negative deviations between techniques. Green zones indicate higher ground elevations on the SfM DSM than in the ALS

grid, red indicate the opposite, and yellow elevation matches. The upstream half domain presented a general tendency of SfM to overestimate elevations on the floodplain, and in turn underestimate them on the terrace. This trend is also observed in the upper part of the downstream reach. Yet, these zones showed exceptions, such as a green patch at the terrace close to the dashed limit, and a red patch on the floodplain at the end of the upstream half reach. Despite the described general opposed behaviour between floodplain and terrace, the downstream reach evidenced two zones with consistent trends across the domain, covering both the floodplain and terrace. First, lower SfM elevations at the end of the largest embayment (downstream half reach), and second, SfM higher elevations at the end of the reach, before the dashed limit.

Figure 8 presents the relative frequency distributions of the elevation differences divided into three regions: the grassy floodplain, the steep bank, and the bare-ground terrace. Over the grassland, both SfM and ALS had rather similar results (Fig. 8, centre left), with 1 cm a zero mean difference and 3 2 cm of standard deviation (Table 3). On In the contrastry, the bank had a bias between the techniques of 6 cm (Table 3) and a relatively high standard deviation of the same value. Finally, the terrace showed a slightly higher deviation than similar results to those over the grassland regarding the deviation (Fig. 8 and Table 3) but with a bias of -4 cm. The bank area together with the terrace dominate induce an the overall small negative bias in the elevation difference distributions (Fig. 8, left and Table 3). The former with a small contribution to the total number of measurements and the latter with a greater number but a lower magnitude.
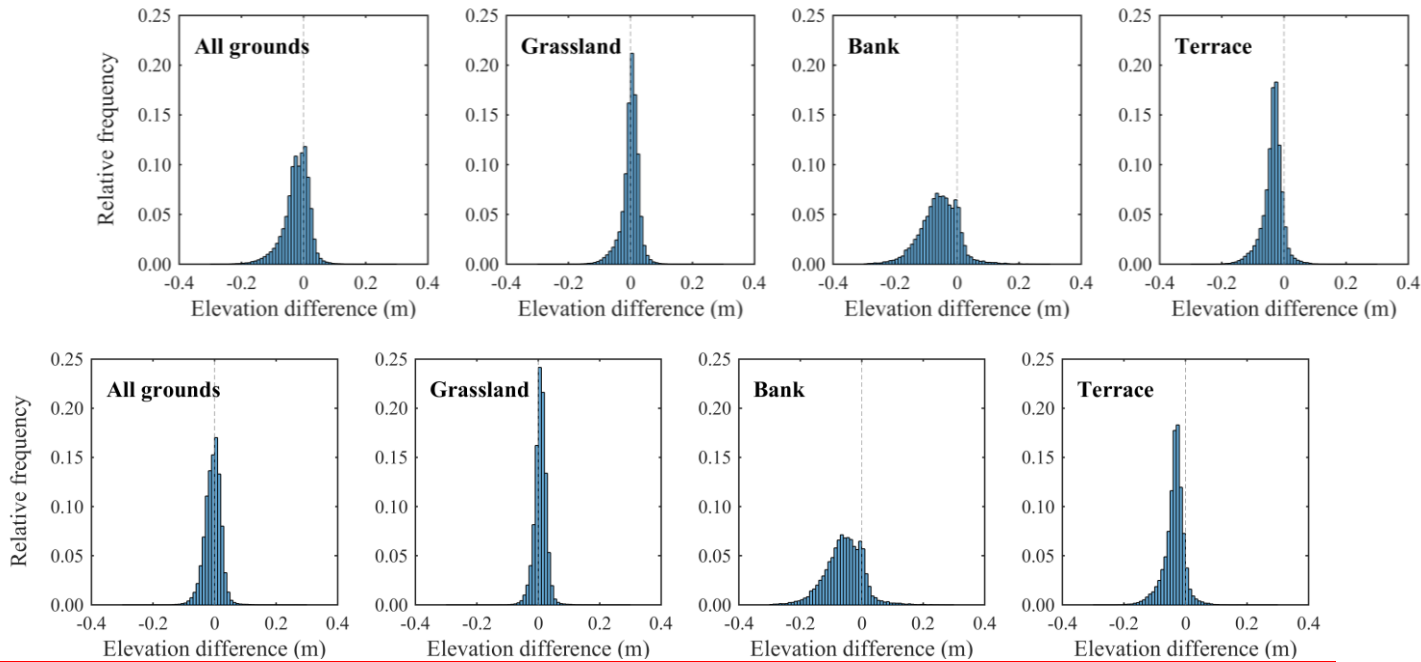

Figure 8: Comparison of elevation differences between SfM and ALS for distinct surface types

Table 3 also indicates the differences of SfM DSM and the ALS with the 129 RTK GPS points. Interestingly, the ALS presented a constant bias of 1 cm across all surfaces, but the standard deviation did change significantly among them: the bank had a standard deviation of 9 cm, which doubled the deviation of the terrace and tripled that of the grassland. While

the SFM DSM had comparable absolute biases than those of ALS, the standard deviations were all respectively lower. Particularly at banks, the standard deviation of the SfM DSM was only 3 cm in contrast to the 9 cm of the ALS, which makes the former approach considerably more accurate than the latter. This could explain the relatively large elevation differences between the two methods in the bank area (Fig. 8, centre right), occurring due to a lower precision of the ALS and not vice versa.

Table 3. Mean and standard deviation of elevation differences between SfM, ALS and RTK GPS. Colour intensity indicates the deviation from zero value with minimum/maximum of ±0.09 m.

Subtraction	-	All grounds	Grassland	Bank	Terrace
SfM - ALS (m)	Mean	-0.01	0.01	-0.06	-0.04
	Std. dev.	0.03	0.02	0.06	0.03
ALS - GPS (m)	Mean	0.01	0.01	0.01	0.01
	Std. dev.	0.05	0.03	0.09	0.05
SfM - GPS (m)	Mean	-0.01	0.01	0.01	-0.02
	Std. dev.	0.03	0.02	0.03	0.02
~~Subtraction~~	~~-~~	~~All grounds~~	~~Grassland~~	~~Bank~~	~~Terrace~~
~~SfM - ALS (m)~~	~~Mean~~	~~-0.02~~	~~0.00~~	~~-0.06~~	~~-0.04~~
	~~Std. dev.~~	~~0.04~~	~~0.03~~	~~0.06~~	~~0.03~~
~~ALS - GPS (m)~~	~~Mean~~	~~0.01~~	~~0.01~~	~~0.01~~	~~0.01~~
	~~Std. dev.~~	~~0.05~~	~~0.03~~	~~0.09~~	~~0.05~~
~~SfM - GPS (m)~~	~~Mean~~	~~-0.01~~	~~0.01~~	~~0.01~~	~~-0.02~~
	~~Std. dev.~~	~~0.03~~	~~0.02~~	~~0.03~~	~~0.02~~

4.3 DSM rotation around GCP axis

A regression line was computed with the locations of the GCPs to analyse with respect to this axis the rotational tendency of the model. The GCP distribution around the regression line and the bankline are shown in Fig. 9 (left). The adopted GCPs spanned 19.7 m across the reach and 1.6 m in the vertical direction (Fig. 9, right). The bank scarp along the reach, which is the target survey area, covered 26.9 m in cross-sectional direction due to the wide-ranging erosion magnitudes of the case study, with maximum bank heights of 3.5 m, indicated with a grey area in the right panel of Fig. 9. This side perspective of the domain evidences the potential plane of rotation, whose stability depends on the position of the GCPs.
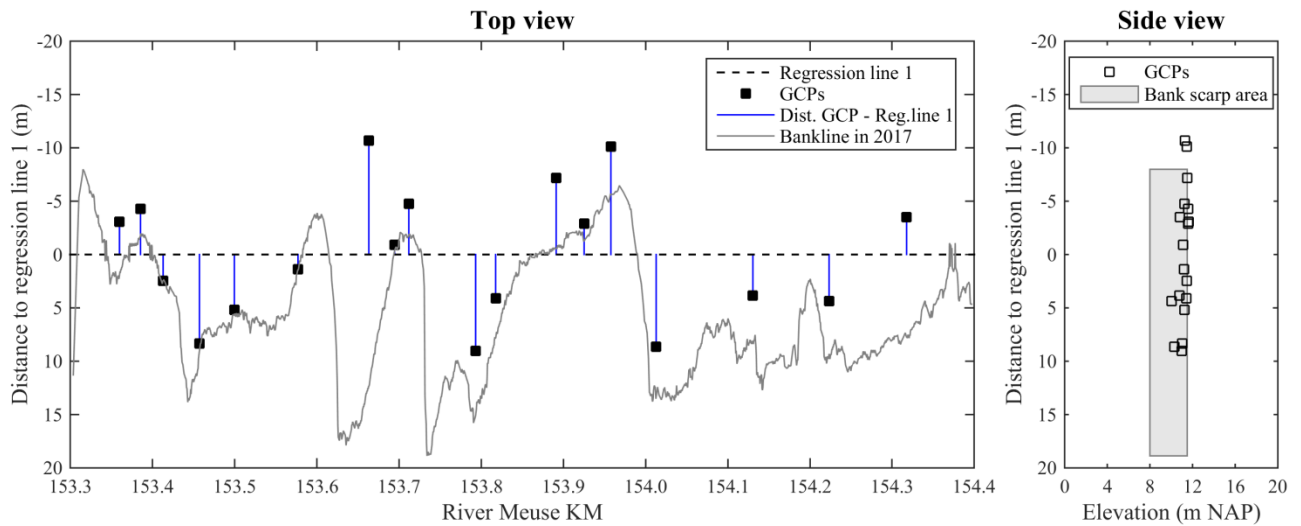
Figure 9: GCP horizontal distances to regression line (left) and respective positions in potential rotation plane from the regression line (right)

The rotation potential of the model is evaluated comparing SfM DSM elevations with those of the 129 GPS points (Fig. 4). Fig. 10a presents the locations of the GPS points used for accuracy control projected at the potential rotation plane, showing that they covered the domain across the channel (abscissa axis) and different elevations along of the scarp area (ordinate axis), resulting in a reasonable sample to assess the model georeferentiation stability. Fig. 10b presents the DSM elevation errors distributed across the regression line 1. In this plane, a second regression line was computed with all 129 points, represented with a dashed black line in Fig. 10b. This line is tilted from the horizontal suggesting that the model was rotated with a magnitude equal to the respective slope.
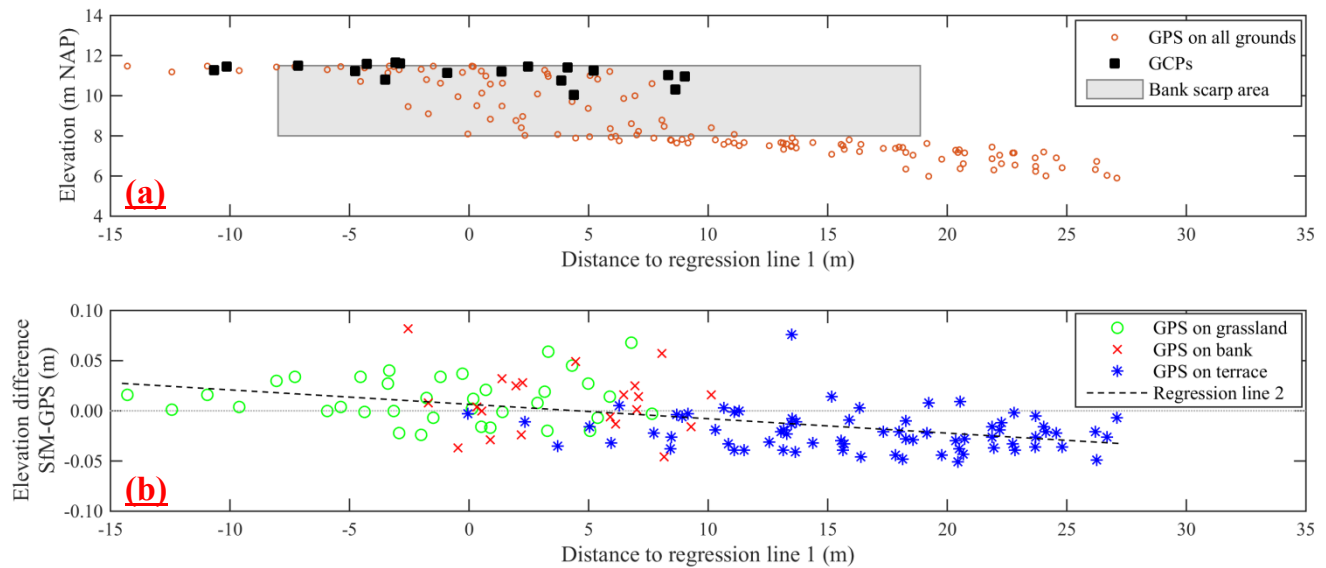
28

Figure 10: a) Location of GPS measurements in potential rotation plane around regression line 1. b) SfM DSM elevation errors across regression line 1, distinguished among areas of grassland, bank and terrace.

The GPS points corresponded to difference surface types, shown with different point markers in Fig. 10b. It is clear that on the left side to the regression line 2 down-crossing, errors mostly had a positive bias, whereas on the right they mostly presented a negative bias. At the same time, those errors with positive bias were generally over a ground covered with grass, and those with negative trend were measured on a slightly sloped bare ground (see also Table 2, column for Test 3). Then, this tendencies could also be ascribed to the overestimation of the grass cover in the former case, and a non-linear transverse deformation beyond the GCP bounds, for the latter. Regardless of the causes, the results showed an overall transverse DSM inclination with respect of the GPS points used for accuracy control. The regression line 2 when evaluated at the extremes of the bank scarp area (-7.99 m and +18.87 m) yielded an elevation difference between these points of 3.9 cm.

4.~~3~~4 Bank erosion features and process identification

Six bank profiles were selected among those surveyed with GPS on January 2017 (~~see~~ Fig. 4) to compare the bank representation with the different survey techniques. Fig. ~~9~~11 shows the bank profiles at ~~Sections~~ sections 1, 2, 4, 6, 7 and 8. These sections presented distinct erosion magnitudes and features after seven years of restoration, for example, ~~Section~~ section 8 (Fig. 4 and ~~9~~11) appeared close to the original condition, with a mild slope and nearly no erosion, whereas ~~Sections~~ sections 6 and 7 had vertical scarps. The SfM DSM profiles are represented by continuous lines, the ALS profiles with dashed lines, and GPS points with circles. The SfM representation had better proximity to the GPS points than the ALS in

almost all cases. What is more, ALS generally overestimated the elevation corresponding to the GPS points, which confirms the bias observed in the comparison of bank elevations shown in Fig. 7 and 8.

SfM profiles showed detailed bank features, such as a collapsed upper bank laying at the toe (~~Section~~ section 2), an overhang at the bank top (~~Section~~ section 1), small-scale roughness on scarps (~~Sections~~ sections 6 and 7), and slump-block deposits (~~Section~~ section 4). These features appeared as simple shapes in the profiles but they were confirmed with field observations. The ALS depicted simpler profiles, smoothed by coarser resolution, which made it difficult to identify characteristic features of the erosion cycle in them. Yet, ALS profiles had enough point spacing to capture gentle bank slopes with reasonable precision (~~Section~~ section 8), but for steeper ones (~~Sections~~ sections 1, 2 and 4) and specially at scarps (~~Sections~~ sections 6 and 7), this technique provides lower accuracies.
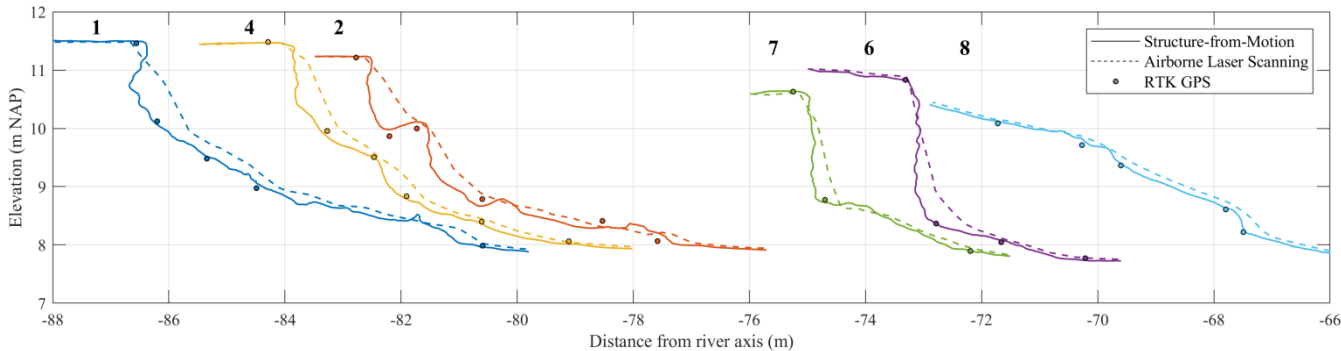

Figure ~~9~~11: Banks measured with SfM (continuous lines), ALS (dashed lines) and GPS (circles) on 17–18 January 2017. Cross-sections are located from left to right, at river km. 153.4, 153.9, 153.5, 154.2, 154.1, and 154.3 (see Fig. 4 for locations).

The temporal development of ~~Section~~ section 4 (Fig. 4 and ~~9~~11) is illustrated in Fig. ~~10a~~12a by a sequence of SfM-UAV surveys. The initial stage corresponds to the survey of Fig. ~~9~~11 on 18 January 2017. The consecutive surveys showed the evolution of the vertical bank profile, through which different processes can be inferred. The bank profile, initially characterized by a top short scarp and slump blocks along the bank face, experienced a mass failure and a further removal of blocks between January 18 and March 15 2017. Between March 15 and April 26, only toe erosion occurred. By June 21, another mass failure happened, which left slump blocks along the lower half of the bank. On July 19, these blocks were removed, leaving a steep bank face. Then, further toe erosion caused a small soil failure at the lower bank whose remains laid at the toe. On October 11, this wasted material was removed. Then, until the last survey on November 22, entrainment occurred at the lower half of the bank profile, further steepening the bank. In light of the results, the methodology resolution and accuracy are high enough to identify different phases of the erosion cycle, enabling the analysis of bank erosion processes in conjunction with data on potential drivers.
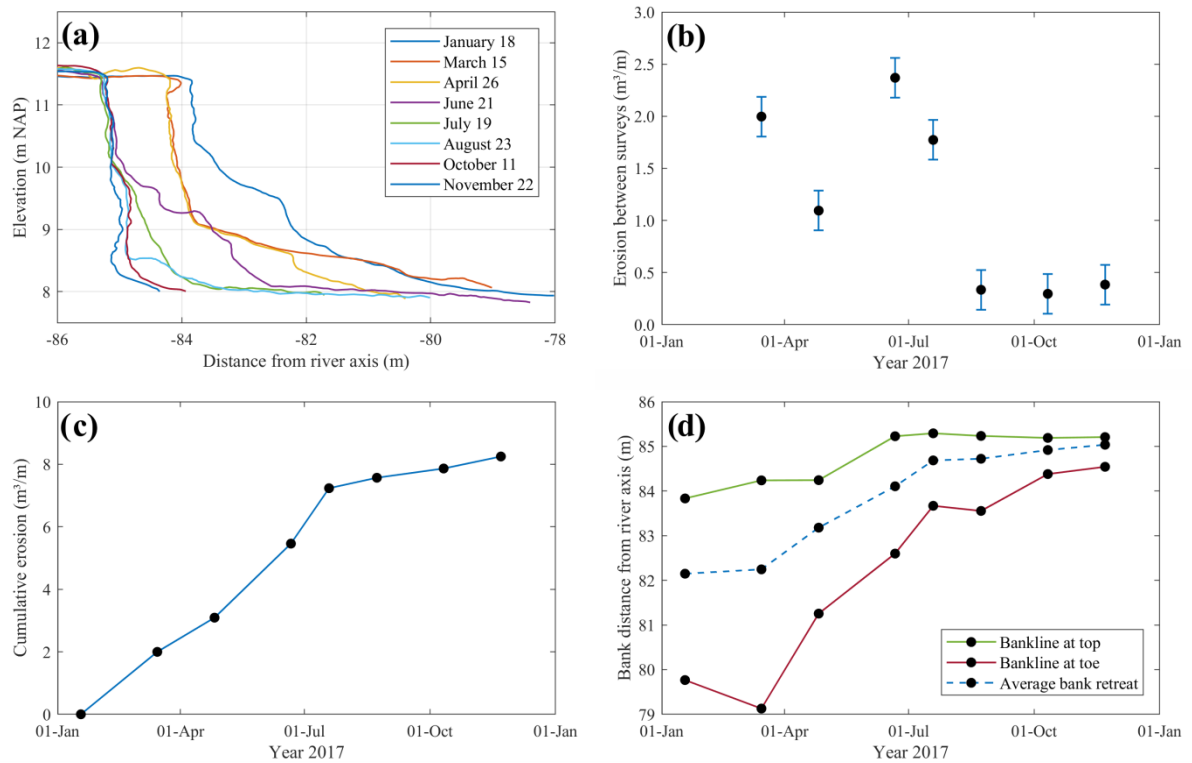
Figure ~~10~~12: Sequential surveys at cross section 4, Meuse River km. 153.9, over 2017. a) Bank profiles from DSMs; b) Eroded volume per unit width between consecutive surveys; c) Cumulative erosion along surveys; d) Bankline locations at the top and toe of the bank.

5   In addition to process description, the quantification of eroded volumes is possible computing the net area between sequential bank profiles. For example, Fig. ~~10b~~ 12b shows eroded volumes per unit width between consecutive surveys plotted at the end of each time interval, with an error bar based on the RMSE of test 3. Evidently, there were different erosion rates during the year and the highest ones happened in the first part of it. Fig. ~~10c~~ 12c presents the respective cumulative eroded volumes per unit width, where the two trends can be distinguished: a gentle slope towards the end and

10 higher rates of sediment yield during the first haft of the year. Given that the topographic measurements are limited to a single year, it is not possible to state whether this behaviour in recurrent on a yearly basis. However, this case exemplifies the possibilities to quantify eroded volumes throughout different phases of the erosion cycle.

      The bankline retreat as a measure of bank erosion involves the identification over time of the bank top, but this concept could be extended, for instance, to the bank toe. Fig. ~~10d~~ 12d shows the temporal progression of the bankline

15 distance from the river axis for both the bank top and the toe, which we arbitrarily defined for this case at 11.1 m and 8.1 m, respectively. The top bankline showed a mayor jump between April and June and a smaller one between the first two surveys, corresponding to mass failure events. The bank toe presented a more gradual retreat, with events of slumping and

temporal accretion that were timely captured along the surveys. This alternative bank retreat representation provides evidence of the development of bank erosion at every survey. The contrast of bankline retreats at the top and toe of the bank illustrates how different processes on their own represent dissimilar erosion evolutions, since they constitute different phases of the erosion cycle, i.e. at the top mass failures and the toe slump block removal and entrainment. Finally, the average bankline between bank toe and top would best represent the real retreat (dashed line in Fig. 10d12d), despite not necessarily indicating an actual bank location for a specific elevation. This approach logically considers all erosion phases and follows a similar trend as the cumulative erosion of Fig. 10e12c.

Figure 13: Zoomed-in UAV photos from track 1 at section 4, km. 153.9, showing diverse bank erosion stages: slump blocks at bank toe on June 21 (left), clean bank face after block removal on July 19 (centre), and undermining on August 23 (right).

Finally, the availability of the UAV imagery provides additional information to analyse and interpret bank evolution through direct observation. Figure 13 shows photographs from the three consecutive surveys on June 21, July 19 and August 23 at section 4, km. 153.9. At this bank area, the sequence shows on the left side of the panels only entrainment at the bank toe, and from the centre (km. 153.9) to the right, one or more erosion cycles. Cross section 4 presented on June 21 (Fig.13, left panel) slump blocks laying at the bank toe that were removed by July 19. Then on August 23, this cross section had incipient undermining at the lower bank and block deposition at the toe. The bank area at the right of section 4 experienced a second mass failure after June 21, completing one erosion cycle, and further downstream it is more difficult to keep track of the cycles due to faster erosion rates. The UAV photos also evidence the progressive growth of grass over the floodplain, especially observable next to the walking path, which was captured along the surveys (Fig. 12a).

5 Discussion

5.1 UAV flight and SfM precision

In general, there were no large differences in accuracy between the DSMs derived with different photo perspectives and overlaps. The accuracy of the tests, except for test *4*, was approximately 10 cm complying with the target accuracy and resolution of 14 cm, and they all had sufficient resolution to represented characteristic features of the erosion cycle, such as slump block deposited at the bank toe and mass failures. Yet, other topographic features that were hidden from the nadir UAV perspective, such as undermining, were only captured from oblique camera perspectives. For instance, the area below

32

the top overhangs visible at cross sections 1 and 2 (Fig. ~~9~~11) were not captured in test *2,* and were represented with a lower resolution in test *4*. The UAV viewpoint of track 1 not only had the largest bank area coverage compared to the other camera perspectives proposed in this work, but also achieved the highest elevation precision without the need of other tracks. Yet, the nadir view of track 2 contributed to cover an additional bank area behind trees and bushes growing at the bank toe along the first 200 m of the reach (Fig. 2, left), for which it was complementarily used with track 1. Since vegetation can occlude the bank face, if denser and more abundant, it could prevent the usage of the survey technique, in a similar way as high water levels do.

The results herein show that, in the absence of bank toe vegetation, a single oblique UAV track with eight photo overlaps and visible GCPs appears effective to survey banks with the highest precision and coverage, for the given sensor size and resolution, camera-object distance and lighting conditions. This number of photo overlaps agrees with the laboratory experiment of Micheletti et al. (2015), who found that above eight the mean error was only slightly decreased, in contrast to increasing overlaps within the range below eight. Nevertheless, they showed that overlaps higher than eight reduced the number of outliers, a trend which in our case is evident for less overlaps: test *1c* (4 overlaps) mainly differed from test *1b* (8 overlaps) in a higher RMSE but not in the mean. This difference may arise from the distinct texture and complexity of each surface, which presumably requires different number of images for a similar performance (James and Robson, 2012; Westoby et al., 2012; Micheletti et al., 2015).

A RMSE of ~~3 cm (more precisely~~ 2.8 cm~~)~~ to measure a riverbank with the photo combination of test *3* results in a relative precision with respect to the average camera-surface distance of 0.0007 or ~1:1400. This relative precision ratio is somewhat higher than ~1:1000 achieved by James and Robson (2012) for steep irregular features at kilometre-scale in a volcanic crater and decametre-scale in a coastal cliff, whereas our precision is somewhat lower than ~1:2000 those authors proved at metre-scale. More precise results could be possible using a bigger and higher-resolution sensor, flying closer to the bank, or even trying other oblique bank perspectives. However, this endeavour would only be reasonable if such data are needed for ~~the~~ research purposes and if GCP positioning had also according higher precisions, since registration errors translate into the DSM accuracy during camera parameter optimization and/or georeferentiation (Harwin and Lucieer, 2012; Javernick et al., 2014; Smith et al., 2014).

A precision of 10 cm has implications for the representation of small-scale features at bank scarps. Despite the presence of features in the order of decimetres, we could not assess their accuracy given the discrete GPS points and the 0.5 m ALS grid used to assess the DSM precision. For instance, Fig. ~~10a~~ 12a shows an upper bank scarp along the last four surveys that, if assumed unchanged, it would indicate a maximum distance of 20 cm between surveys, which still would remain within the ±10cm error estimated by the GPS comparison. Although these differences could have been caused by weathering processes or growing grass on the bank face, potential sources of error at such scale could be given, for instance, by registration errors or occlusions caused by the surface roughness (Lague et al., 2013). Then, further research is needed to evaluate the precision at the roughness scale to, for example, analyse form drag at the bank face (Leyland et al., 2015).

The analysis made for test 3 on model rotation evidenced a linear trend with increased surface elevations on the floodplain side of the domain and decreased elevations on the main channel side (Fig. 10b). This tendency was probably caused by a rotation of the DSM around somewhat aligned GCPs that may lead to co-linear solutions of the Helmert transformation (Carbonneau and Dietrich, 2017). Yet, the areal SfM-ALS comparison within ± 5 cm range (Fig. 7b), did not evidence a clear axis along the whole domain that could suggest a rigid rotation of the DSM, since the ALS did have a constant mean accuracy across all surface types (Table 3). The linear rotation tendency, then, might have been obscured by the error range that was larger across the domain (Fig. 6 centre left and 10b) than the mean rotation magnitude, whose elevation difference between the extremes of the cross-sectional domain was 6 cm, and 4 cm within the bank area. Thus, other sources of error were also present that resulted in the obtained error range.

The comparative analysis of the DSMs elevation errors from different photo combinations showed that the ground surfaces surveyed in the case study had different precisions. The grassland presented similar errors with a positive bias throughout all tests. The positive elevation differences are typical of vegetated surfaces (Westoby et al., 2012; Micheletti et al., 2015), whereas the similar performance of different photo combinations might be due to the presence of sufficient and well distributed GCPs in this area (the floodplain). The terrace at the toe of the bank, in contrast, presented different error skewness throughout the tests, which affected the error distribution for all grounds. Interestingly, the error deviation of tests 1 increased as the overlaps decreased, which in turn implies that more overlaps created more robust models. The linear errors cannot explain this behaviour because the same GCP locations were used for all tests, and only the camera parameters were optimized for each.

The error skewness at the terrace throughout the tests can could be related to the fact that this areae terrace was the most distant area from the GCPs and it was not surrounded by them, so that errors in lens distortion corrections could have especially increased here (James and Robson, 2014; Javernick et al., 2014; Smith et al., 2014). This effect was clear at the reach extremes (Fig. 7), where the elevation differences increased with respect to the ALS survey further from the GCPs, for which it is called 'dome' effect. This DSM distortion beyond the GCP surrounding area might affect the bank too when using the GCPs only on the floodplain and not on the bank. In the case study, care was taken to sparsely place the GCPs across the floodplain and at different elevations when it was possible, so that the control points were distributed over the three spatial dimensions as much as possible to increase the georeferencing accuracy (Harwin and Lucieer, 2012). While James and Robson (2014) showed that using different (convergent) camera angles is effective to mitigate the 'dome' effect, our results showed that the DSM precision with eight photo overlaps along a single UAV track did not substantially improve by adding the extra perspective of track 2. This may imply that the chosen number of overlaps and used GCPs were sufficient to avoid such distortions in the bank area that exceed the required accuracy, together with the fact the track had oblique and not nadiral perspective. Moreover, even though direct georeferencing is a promising step forward to minimizing the SfM requirements through more accurate camera calibration (Carbonneau and Dietrich, 2017), GCPs are currently necessary for highest precision by model optimization, georeferentiation, and quality verification.

34

It is most likely that all the mentioned types of error were present in the SfM DSM, i.e., linear errors given by rotation (linear trend of errors across potential rotation plane, Fig. 10b), non-linear errors given by the estimation of camera parameters (patches of higher or lower SfM elevations across the domain compared to ALS, Fig. 7b), overestimation of ground elevation with grass cover (Table 2, Fig. 7b, Fig 12a), and random errors given by the bundle adjustment that could not be assessed herein. Although, the adopted workflow was effective to measure bank erosion processes with the target accuracy, linear and non-linear errors could have been reduced, for instance, using a larger cross-sectional GCP distribution or better visible and bigger GCP targets. Other possibilities are also open, such as combining two oblique perspectives with a second angle better capturing the floodplain, GCPs and bank area.

5.2 Comparison of two reach-scale techniques: SfM and ALS

The elevation bias at the bank between the SfM-based DSM and the ALS grid (Fig. 8) was caused by the topographic overestimation of ALS (Table 3 and Fig. 9). This ubiquitous error is ascribed to a known limitation of ALS systems related to the laser beam divergence angle, which locates the closest feature within the laser footprint at the centre of the footprint. This increases the ground elevation at high-slope areas (Bailly et al., 2012), which is the case for riverbanks. Still, the ALS resolution and precision were enough to identify bank slopes, in accordance with other studies (e.g., Tarolli et al., 2012; Ortuño et al., 2017). Furthermore, despite the ALS capability to estimate volume changes of eroded banks (Kessler et al., 2013), the method omits information related to the phases of the erosion cycle by not surveying erosion features smaller than its resolution (in this case 0.5 m), apparent in contrast with SfM profiles (Fig. 911). Moreover, if finer ALS resolutions are available, for instance using higher frequency lasers or working with the raw data, more ground details can be captured, but still vertical or undermined profiles would be missed.

The elevation differences between the methods observed for grassland (Fig. 8, centre left) were probably caused by dissimilar ground resolutions, because a larger elevation scatter is expected in the SfM-based DSM when capturing grass with 2 cm resolution, whereas compared to the interpolated ALS had samples into a spaced 50 cm grid, even when derived from froma 0.16 m beam comparable footprints size. Nonetheless, the mean difference was zero (Table 3), so that both methods overestimate in the same way the real ground elevation due to grass cover. The effect of this is visible, for instance, in the increasing surface elevations on the floodplain over a year (Fig. 10a12a), which happens after the mowing period in October. The terrace at the bank toe presented a similar scatter as grassland, but had a small negative bias that could be explained by a DSM rotation or a slight transverse 'dome' effect of the SfM DSM.

The distance covered by the SfM-UAV method depends on the flight autonomy. The deployed UAV had autonomy of approximately 25 minutes, which limited the maximum bank survey extent to approximately 2 km for the tested UAV height and speed, and camera resolution and shutter frequency. This practical limit will change with the progressive development of UAVs, but the distance covered by a single flight is currently significantly smaller than the one covered by ALS. Although a larger camera-object distance and speed than the used in this work would increase the surveyed area,

35

decreasing the ground resolution and the UAV stability may result in the loss of sufficient detail to capture erosion features, and what is more, decrease the DTM precision that depends on the image scale (James and Robson, 2012; Micheletti et al., 2015). Therefore, further investigations would be required to explore the practical limits of UAV-bank monitoring in views of extending the survey coverage.

5.3 UAV-SfM challenges to measure bank erosion processes

The use of UAV-SfM to measure bank erosion processes presents specific challenges, since bank areas usually have vertical surfaces and lengths can be much larger than the other two dimensions. Furthermore, the reach under analysis was particularly straight, introducing additional complexity to apply the technique.

5.3.1 Vertical surfaces

The bank presented very steep, vertical and undermined surfaces that required an oblique camera perspective to adequately capture it. On the other hand, a camera from a top view omitted undermined areas and reduced the DSM resolution at the bank. It was then necessary to include an oblique UAV camera in the flight plan to measure bank erosion at the process scale, but in turn this required that GCPs needed sufficient visibility from this angle. In addition, it was convenient to have accessible GCP in the field for their placement and sometimes later removal, so their location across the bank became important too, from a practical point of view.

The accessibility and visualization of GCPs depend on where and how they are placed across the bank profile. In our adopted approach, GCP targets were horizontally placed over the floodplain and close to the bankline, covering 20 m across the channel, which was convenient for a fast field campaign. Yet, GCPs were not placed at the bank toe or over the bank face, so a very limited vertical extent was covered (Fig. 9-10), and at the same time, the target area was not surrounded by GCPs along the three dimensions. Then, the rotation stability of the DSM and the non-linear effects beyond GCP bounds relied on the horizontal, and particularly the cross-sectional, GCP distribution, as well as on the number of photo overlaps that reduced the error scatter (see Sect. 5.1). Although a larger vertical range, as with GCP at the bank toe, may be effective to reduce potential non-linear errors at the bank, the linear errors may not significantly be reduced in this way given the relatively short bank height (~3.5 m) and corresponding horizontal extent. In contrast, the relatively large cross-sectional GCP span possible on the floodplain (e.g., 20 m) is clearly more effective to avoid model rotations around the GCP axis (see Fig. 9). Finally, in our case study, there were no clear non-linear effects at the bank area that could justify the placement of GCPs along the bank face.

The visible dimension of the GCP is proportional to the cosine of the viewing angle with respect to the normal of the plane in which the GCP lies (say α), which increased the uncertainty to locate the target centre along the transverse direction, thus hindering the model georeferentiation when a single UAV track was used. On the other hand, targets were not always distorted in longitudinal direction from oblique angles, i.e., when the camera was near the GCP cross-section, so horizontal errors were not as sensitive along the river axis as they were across the channel. Linear positioning errors in the

transverse direction directly affect the accuracy to quantify erosion rates since this is based on the change of bank face positions over time. Moreover, the error introduced by a coarser resolution translated into elevation errors, and these directly affect rotational errors. On the other hand, the lateral view helped to compensate for this, since this elevation errors decreased with the cosine of α. Although the proposed approach attained the required DSM accuracy, the mentioned shortcoming could been solved by orienting the GCP plaques towards the oblique camera, placing them somewhat parallel to the bank surface. This could have been done, for instance, with a back stand on the rigid plaques.

5.3.2 Linear domain

Banks, considered from the reach scale, are linear domains that extend along the river with the other two dimensions much shorter than their length. The application of UAV-SfM to these particularly elongated domains run the risk of having rotated solutions of the Helmert transformation when georeferencing the DSM with GCPs. The proposed workflow intended to avoid linear rotations of the DSM through sufficiently accurate and well-distributed GCPs, while using parallel UAV tracks along the river, which did not contribute to the model stability. As discussed in Sect. 5.1, the cross-sectional GCP distribution and the accuracy of GCPs were essential to achieve the desired DSM accuracy by reducing linear and also non-linear errors, which depended on both the field measurement and the identification in the photographs.

The choice of UAV tracks parallel to the river axis simplifies the mission set up and shortens the flying time too. Yet, this configuration does not provide additional stabilization to the DSM because it is closely aligned with the potential axis of rotation. For instance, the combination of flight tracks that covered a wide cross-sectional distance could contribute to reduce the model rotation through the locations given by the UAV internal GPS (Carbonneau and Dietrich, 2017). Nonetheless, such approach would be limited by relatively high GPS errors for the accuracy needed to measure bank erosion processes. Thus, this method would require large distances between tracks across the floodplain to significantly reduce the influence of those positioning errors on the model rotation. The adopted approach relied on GCPs to georegister the DSM, which proved effective despite using parallel-axes image orientations. What is more, since parallel UAV tracks tend to increase doming effects (James and Robson, 2014), GCPs were also important to prevent excessive non-linear errors for the required accuracy. Fig. 7b showed no significant DSM deformations within the GCPs, but increasing errors outside the GCP bounds, for which they need to be carefully distributed.

In principle, the cross-sectional GCP distribution should be as wide as possible to ensure that the model georeferentiation is stable. Then, a set of GCPs should be placed close to the bankline, which is also beneficial to reduce non-linear errors at the bank area and to visualize them from the oblique camera, and another set far away from the bankline. This second group, on the other hand, would have lower resolutions in the UAV photos due to larger distances to the camera, and higher related elevation errors during the target identification on the images. A compromise is then necessary between a minimum GCP cross-sectional span and the target resolution, especially for a flight plan with a single oblique UAV path. In our case, a GCP distribution spanning 20 m across the floodplain satisfied the required DSM accuracy of 1/25 the bank height, but improvements are possible in this respect.

For instance, if the first GCP line is 40 m from the UAV camera in oblique direction (Fig. 3b), the second line could be placed 51 m inland from the first line to be 80 m from the UAV sensor (twice as far), but with targets four times as big as those next to the bankline to linearly compensate for the decrease in the image resolution (although no linear trend was found between errors and sensor-object distance, Eltner et al., 2016). In this example, the rotational error would decrease 2.5 times compared to the results presented here, given by the increase in the cross-sectional GCP footprint and considering similar elevation errors (from GPS and image identification). Finally, as indicated in the previous section, it is advisable to use inclined targets perpendicular to the line of sight of the camera, which could have double spacing compared to those in the front while keeping the number of photo overlaps that capture them. This method would require more time in the field to place and measure GCPs but certainly would achieve higher DSM accuracies from lower linear errors.

5.3.3 Other considerations

A single oblique path was sufficient to achieve the highest accuracy among the different tests (Sect. 4.1), but using only this track when there is no bank-toe vegetation would still present a challenge to georeference the DSM, as already discussed. In this work, we opted to use both oblique and nadiral perspectives because of the presence of bank-toe vegetation and to benefit from their respective advantages, i.e., larger coverage and higher resolution at the bank from oblique view and higher resolution to recognize distant GCPs from top view. Yet, a single oblique path could be utilized to optimize resources with improvements to the adopted approach (see previous Sections). In addition, other factors are relevant aiming at reducing errors as much as possible, such as choosing non-reflective materials for GCP targets, flying on overcast and bright days, using automated GCP identification algorithms, etc.

In our approach, GCPs were manually identified in the photographs based on three concentric geometries: the inner and outer circles of the CD reflective area and the tile perimeter. The centre of these geometries was estimated depending on the camera-GCP distance, which defined the target resolution, and the light reflexion intensities of each case. Then, fast flipping through photo focusing on single GCP at a time (with the PageUp / PageDown keys in PhotoScan) helped to adjust the estimation of the target centre, which turned consistent the location of the GCP among all camera views. The errors introduced during the target identification affect the georeferentiation, and although errors may compensate if not systematically biased, their influence is higher the narrower the cross-sectional GCP span due to the rotation tendency of elongated domains. This source of error may be reduced with wider GCP patterns than the used in our approach, but also through other improvements-, such as automated identification of GCP and Monte Carlo tests (James et al., 2017), to identify more accurately the GCP and optimize the number of GCP and minimize DSM errors.

Finally, camera settings were automatic, being adjusted by the light conditions during the flight. But, the camera could be manually set to optimally capture the texture of the bank scarp. In this respect, GCP targets should ideally have a similar reflecting surface to project to the camera a similar amount of light for their later identification. A tilted target would also contribute to have similar reflecting conditions after comparable orientations to the bank with respect to the sun. Furthermore, if the date of the survey campaign is flexible, then overcast but bright days are advisable whenever possible.

This is to avoid overexposed or underexposed bank areas due to direct sun light and shades that result in lower image textures within each of these zones and thus in a lower number of detected image features (James and Robson, 2012; Gómez-Gutierrez et al., 2014a). For example, note in the central photo of Fig. 13 that there were no textural differences due to shades but only due to the bank surface.

5.3 4 Surveying bank erosion

Sequential surveys allowed to capture different phases of the erosion cycle (Fig. 12a), which demonstrates that quantitative detection of processes is feasible. Previous studies on bank erosion proved the capabilities of SfM for post-event analysis (Prosdocimi et al., 2015), e.g. representing block deposition, or for 2.5D bank retreat quantification (Hamshaw et al., 2017), whereas herein all erosion phases were sequentially captured, demonstrating the 3D potentialities over the complete process of erosion. Of course, the ability to monitor banks at the process scale depends on the time interval with which the method can re-survey the exposed part of banks and will only cover pre- and post-flood conditions. The survey frequency and the duration of a full cycle of erosion determine the temporal resolution with which the development of processes is captured. Then, the bank retreat rate of each case determines the necessary frequency of surveys to capture erosion processes within a single cycle. Bank erosion rates naturally depend on each site, after different river sizes, hydraulic conditions, bank materials, etc. which Iin the presented study site erosion rates varied enormously (Fig. 3), but s Still, the performed eight surveys within a year successfully captured bank processes within a single erosion cycle in areas of fast retreat such as Section section 4.

The study site with a regulated water level and recently restored actively eroding banks was a perfect example for the application of this technique, because banks were exposed and erosion rates were compatible with the proposed average sampling frequency of six weeks. For other types of rivers, where erosion mainly occurs during floods when banks are not exposed, this method would allow measuring pre- and post-event conditions only. Given the high resolution achieved, the method is applicable to all river sizes. However, due to the accuracy obtained, the application is only advised in cases where bank retreat is larger than approximately 30 cm between consecutive surveys.

Erosion processes happening at small spatial scales, such as weathering, would be hardly or not measurable with the precision achieved in this investigation.. For this, other methods are already available, for instance TLS and boat-based laser scanning, that provide higher precisions (mm before registration errors, e.g., O'Neal and Pizzuto, 2011) and comparable resolutions (cm, e.g., Heritage and Hetherington, 2007). In addition, close-range terrestrial photogrammetry can also offer the necessary precision for such endeavours, e.g., from a tripod (Leyland et al., 2015) or a pole on the near-bank area (Bird et al., 2010), at the expense of covering shorter bank lengths. Another alternative are erosion pins, which may also provide higher accuracies, yet with point resolution.

UAV-SfM appears a suitable survey method for both process identification and volume quantification in bank erosion studies, given the decimetre precision range with 3 cm RMSE and the 3D high resolution achieved with a low-cost UAV. As Resop and Hession (2010) suggested, high-resolution three-dimensional capabilities offer great possibilities when

spatial variability of retreat is critical compared to traditional cross-profiling methods. In addition, the reduced deployment time of UAVs in the field is advantageous in relation to cross-profiling, while it also improves identification of complex bank features (Fig. 11) and volume computations as other 3D high-resolution techniques (O'Neal and Pizzuto, 2011). Nonetheless, UAV-SfM require longer post-processing times at the office, which should not be underestimated (Westoby et al., 2012; Passalacqua et al., 2015).

5

This technique remains low-cost compared to TLS or MLS, for which it is more convenient for cases where roughness is beyond the scale of interest, and target bank lengths are smaller than 3000 m. This would approximately be the longest distance for a single UAV flight in our case study. For longer reaches, MLS would then compete with UAV-SfM from a practical perspective, since more than one survey/flight would be needed. However, all TLS, MLS and UAV-SfM would have limitations to survey the bank surface in presence of dense bank vegetation (Hamshaw et al., 2017). In these cases, ALS provides an alternative, albeit with significant lower resolution and higher costs (Slatton et al., 2007).

10

For large river extents, i.e., several kilometres, Grove et al. (2013) showed that process inference is possible combining ALS with high-resolution aerial photography, two techniques that are typically applied for eroded volume estimations and bank migration (Khan and Islam, 2003; Lane et al., 2010; De Rose and Basher, 2011; Spiekermann et al., 2017). In that work, the scale of the river (banks higher than 6 m) allowed a spatial resolution of 1 m to capture features that together with photo inspection provided information on mass failure type and fluvial entrainment. To date, UAV-SfM covers smaller extents (Passalacqua et al., 2015), but provides much higher resolutions, allowing for process identification (such as undermining) and more precise volume computations (see Fig. 11 for profile differences between ALS and SfM). For a similar (or higher) accuracy and resolution than those of UAV-SfM and large distances, boat-based laser scanning becomes an attractive, yet more expensive, solution.

15

20

6 Conclusion

This work evaluated the capability of Structure- from- Motion photogrammetry applied with low-cost UAV imagery to monitor bank erosion processes along a river reach. The technique's precision was investigated by comparison with GPS points and an airborne laser scanning. Vertical bank profiles were analysed to identify stages of erosion and infer processes. We used a low-cost UAV with a 12 MP built-in camera, flying 25 m from the least retreated bankline and 25 m above the floodplain level, which took oblique , which produced a photographs set with an oblique perspective andwith at least eight image overlaps at of each bank point. Together withThe distribution of ground-control points across the floodplain avoided excessive linear errors from model rotation, keeping the accuracy within the target of 1/25 times the bank height. Thus, this GCP distribution and image network geometry photo set was enough to generated through SfM a digital surface model with sufficient accuracy and resolution to recognize signatures of the different phases of the bank erosion cycle from the obtained bank profiles.

25

30

40

The accuracy of the DSM constructed with the SfM technique did not significantly increase with more than eight photo overlaps along a single oblique UAV track. The coverage of bank area behind bank toe vegetation, on the other hand, was increased by adding a vertically oriented perspective, albeit without a significant accuracy increase. As a result, banks were surveyed with 2 cm resolution and a 10 cm elevation precision, whose mean was 1 cm and standard deviation 3 cm (~1:1400 relative to camera-object distance, in line with previous SfM topographic applications). This accuracy was confirmed along the river reach ~~after comparison~~ with ~~the~~ airborne laser scanning, although the latter ~~. The SfM based topography agreed well with ALS over horizontal areas, but over bank slopes the latter overestimated elevations~~overestimated elevations over bank slopes. Higher SfM errors were observed in areas beyond the extent of ground-control points, showing that control points should also be placed outside the monitoring reach and close to the bankline. Furthermore, the GCP distribution across the floodplain proved very important to prevent model rotation along GCP axes, so a second line of GCP located further inland is recommended, together with proper targets, to reduce model errors as much as possible.~~area.~~

~~The SfM resolution captured details of the bank face through which features of different phases of the erosion cycle could be identified. A relative elevation precision with respect to the camera-object distance of ~ 1:1400 was obtained, in line with previous SfM topographic applications. The technique's accuracy, resolution and frequency enabled capturing erosion processes over sequential surveys. The survey frequency depends on bank retreat rates, which depend on the river size, hydraulic conditions, bank material, etc.~~

This investigation demonstrates the capabilities of a low-cost UAV to monitor banks at the process scale, while covering a middle-size river reach of 1.2 km long in a single campaign. The combination of UAV and Structure-from-Motion photogrammetry can provide relevant information of the spatial structure of bank erosion processes, and with sufficient frequency of acquisition, represent the temporal evolution of morphological processes within the erosion cycle. This method can also be used to compute eroded volumes throughout different phases of the cycle and analyse the contribution of each mechanism to overall retreats.

The applied technique is most suitable when measuring bank lengths not exceeding ~~the~~ 3000 m, and i~~. Its~~ flexibility, fast deployment and high resolution are especially convenient for surveying highly irregular banks. While t~~This~~ method can survey the full cycle of erosion, and not only pre- and post-event conditions, its~~. The~~ main limitations are dense riparian vegetation and high water levels, as for ~~, but the same applies to~~ most survey techniques.

Data availability

The data utilized in this work will be publicly available at the 4TU repository after the publication of this manuscript.

Author contribution

The field campaigns, data processing, data analysis and discussion of results were carried out by the first author. The writing of the manuscript was done by the first and second authors. The team authors provided expert opinion, refinement of paper writing and figures, and ideas that improved the final quality of this work.

References

10 Alho, P., Kukko, A., Hyyppä, H., Kaartinen, H., Hyyppä, J., and Jaakkola, A.: Application of boat-based laser scanning for river survey, Earth Surface Processes and Landforms, 34(13), 1831-1838, doi:10.1002/esp.1879, 2009.

ASCE Task Committee on Hydraulics, Bank Mechanics, and Modeling of River Width Adjustment. River width adjustment. I: Processes and mechanisms, J. Hydraul. Eng. 124 (9), 881–902, doi:10.1061/(ASCE)0733-9429(1998)124:9(881), 1998.

Bailly, J. S., Kinzel, P. J., Allouis, T., Feurer, D., and Le Coarer, Y.: Airborne LiDAR methods applied to riverine

15 environments, Fluvial remote sensing for science and management, 141-161, doi: 10.1002/9781119940791.ch7, 2012.

Bangen, S. G., Wheaton, J. M., Bouwes, N., Bouwes, B., & Jordan, C. (2014). A methodological intercomparison of topographic survey techniques for characterizing wadeable streams and rivers, Geomorphology, 206, 343-361, doi:10.1016/j.geomorph.2013.10.010, 2014.

Barker, R., Dixon, L., and Hooke, J.: Use of terrestrial photogrammetry for monitoring and measuring bank erosion, Earth

20 Surface Processes and Landforms, 22(13), 1217-1227, doi:10.1002/(SICI)1096-9837(199724)22:13<1217::AID-ESP819>3.0.CO;2-U, 1997.

Bird, S., Hogan, D., & Schwab, J.: Photogrammetric monitoring of small streams under a riparian forest canopy, Earth Surface Processes and Landforms, 35(8), 952-970, doi:10.1002/esp.2001, 2010.

Brasington, J., Rumsby, B. T., and McVey, R. A.: Monitoring and modelling morphological change in a braided gravel-bed

25 river using high resolution GPS-based survey, Earth Surface Processes and Landforms, 25(9), 973-990, doi: 10.1002/1096-9837(200008)25:9<973::AID-ESP111>3.0.CO;2-Y, 2000.

Brasington, J., Vericat, D., and Rychkov, I.: Modeling river bed morphology, roughness, and surface sedimentology using high resolution terrestrial laser scanning, Water Resources Research, 48(11), doi:10.1029/2012WR012223, 2012.

Carbonneau, P.E. and Dietrich, J.T.: Cost-effective non-metric photogrammetry from consumer-grade sUAS: implications for direct georeferencing of structure from motion photogrammetry, Earth Surface Processes and Landforms, 42(3), 473-486, doi:10.1002/esp.4012, 2017.

Cavalli, M., Tarolli, P., Marchi, L., and Dalla Fontana, G.: The effectiveness of airborne LiDAR data in the recognition of channel-bed morphology, Catena, 73(3), 249-260, doi:10.1016/j.catena.2007.11.001, 2008.

Charlton, M. E., Large, A. R., and Fuller, I. C.: Application of airborne LiDAR in river environments: the River Coquet, Northumberland, UK, Earth surface processes and landforms, 28(3), 299-306, doi:10.1002/esp.482, 2003.

Clapuyt, F., Vanacker, V. and Van Oost, K.: Reproducibility of UAV-based earth topography reconstructions based on Structure-from-Motion algorithms, Geomorphology, 260, 4-15, doi:10.1016/j.geomorph.2015.05.011, 2016.

Clark, L.A. and Wynn, T.M.: Methods for determining streambank critical shear stress and soil erodibility: Implications for erosion rate predictions, Transactions of the ASABE, 50(1), 95-106, doi:10.13031%2F2013.22415, 2007.

Cook, K.L.: An evaluation of the effectiveness of low-cost UAVs and structure from motion for geomorphic change detection, Geomorphology, 278, 195-208, doi:10.1016/j.geomorph.2016.11.009, 2017.

Couper, P. R.: Space and time in river bank erosion research: A review, Area, 36(4), 387-403, doi: 10.1111/j.0004-0894.2004.00239.x, 2004.

Couper, P. R., and Maddock, I. P.: Subaerial river bank erosion processes and their interaction with other bank erosion mechanisms on the River Arrow, Warwickshire, UK, Earth Surface Processes and Landforms, 26(6), 631-646, doi:10.1002/esp.212, 2001.

Couper, P., Stott, T. I. M., and Maddock, I.: Insights into river bank erosion processes derived from analysis of negative erosion-pin recordings: observations from three recent UK studies, Earth Surface Processes and Landforms, 27(1), 59-79, doi: 10.1002/esp.285, 2002.

Darby, S. E., Rinaldi, M., and Dapporto, S.: Coupled simulations of fluvial erosion and mass wasting for cohesive river banks, Journal of Geophysical Research: Earth Surface (2003–2012), 112(F3), doi: 10.1029/2006JF000722, 2007.

De Rose, R. C., and Basher, L. R.: Measurement of river bank and cliff erosion from sequential LIDAR and historical aerial photography, Geomorphology, 126(1), 132-147, doi:10.1016/j.geomorph.2010.10.037, 2011.

Eltner, A., and Schneider, D.: Analysis of different methods for 3D reconstruction of natural surfaces from parallel-axes UAV images, The Photogrammetric Record, 30(151), 279-299, doi:10.1111/phor.12115, 2015.

Eltner, A., Kaiser, A., Castillo, C., Rock, G., Neugirg, F., and Abellán, A.: Image-based surface reconstruction in geomorphometry–merits, limits and developments, Earth Surface Dynamics, 4(2), 359-389, doi:10.5194/esurf-4-359-2016, 2016.

Florsheim, J.L., Mount, J.F., and Chin, A.: Bank Erosion as a Desirable Attribute of Rivers, BioScience, 58(6), 519-529, doi:10.1641/B580608, 2008.

Fonstad, M. A., Dietrich, J. T., Courville, B. C., Jensen, J. L., and Carbonneau, P. E.: Topographic structure from motion: a new development in photogrammetric measurement, Earth Surface Processes and Landforms, 38(4), 421-430, doi:10.1002/esp.3366, 2013.

Fukuoka, S.: Erosion processes of natural river bank, Proceedings of the 1st International Symposium on Hydraulic
5 Measurement, Beijing, Vol. 223229, 1994.

Girardeau-Montaut, D.: CloudCompare (version 2.9; GPL software), EDF RandD, Telecom ParisTech, available at: http://www.cloudcompare.org/, last access: January 2018.

Gómez-Gutiérrez, Á., de Sanjosé-Blasco, J. J., de Matías-Bejarano, J., and Berenguer-Sempere, F.: Comparing two photo-reconstruction methods to produce high density point clouds and DEMs in the Corral del Veleta Rock Glacier (Sierra
10 Nevada, Spain), Remote Sensing, 6(6), 5407-5427, doi: 10.3390/rs6065407, 2014a.

Gómez-Gutiérrez, Á., Schnabel, S., Berenguer-Sempere, F., Lavado-Contador, F. and Rubio-Delgado, J.: Using 3D photo-reconstruction methods to estimate gully headcut erosion, Catena, 120, 91-101, doi:10.1016/j.catena.2014.04.004, 2014b.

Grove, J. R., Croke J., Thompson, C.: Quantifying different riverbank erosion processes during an extreme flood event, Earth Surface Processes and Landforms, 38(12), 1393-1406, doi:10.1002/esp.3386, 2013.

15 Hamshaw, S.D., Bryce, T., Rizzo, D.M., O'Neil-Dunne, J., Frolik, J. and Dewoolkar, M.M.: Quantifying streambank movement and topography using unmanned aircraft system photogrammetry with comparison to terrestrial laser scanning, River Research and Applications, 33(8), 1354-1367, doi:10.1002/rra.3183, 2017.

Hartley, R., and Zisserman, A.: Multiple view geometry in computer vision, Cambridge university press, 2003.

Harwin, S., and Lucieer, A.: Assessing the accuracy of georeferenced point clouds produced via multi-view stereopsis from
20 unmanned aerial vehicle (UAV) imagery, Remote Sensing, 4(6), 1573-1599, doi:10.3390/rs4061573, 2012.

Henshaw, A. J., Thorne, C. R., and Clifford, N. J.: Identifying causes and controls of river bank erosion in a British upland catchment, Catena, 100, 107-119, doi:10.1016/j.catena.2012.07.015, 2013.

Heritage, G., and Hetherington, D.: Towards a protocol for laser scanning in fluvial geomorphology, Earth Surface Processes and Landforms, 32(1), 66-74, doi:10.1002/esp.1375, 2007.

25 Hooke, J.M.: An analysis of the processes of river bank erosion, Journal of Hydrology, 42(1-2):39-62, doi:10.1016/0022-1694(79)90005-2, 1979.

Immerzeel, W. W., Kraaijenbrink, A., Shea, J. M., Shrestha, A. B., Pellicciotti, F., Bierkens, M. F. P., and De Jong, S. M.: Highresolution monitoring of Himalayan glacier dynamics using unmanned aerial vehicles, Remote Sens. Environ., 150, 93–103, doi:10.1016/j.rse.2014.04.025, 2014.

30 Jacobson A. et al.: Geometry Processing Toolbox, available at: http://github.com/alecjacobson/gptoolbox, last access: January 2018.

James, M. R., and Robson, S.: Straightforward reconstruction of 3D surfaces and topography with a camera: Accuracy and geoscience application, Journal of Geophysical Research: Earth Surface, 117(F3), doi:10.1029/2011JF002289, 2012.

James, M. R., and Robson, S.: Mitigating systematic error in topographic models derived from UAV and ground-based image networks. Earth Surface Processes and Landforms, 39(10), 1413-1420, doi:10.1002/esp.3609, 2014.

James, M.R., Robson, S., d'Oleire-Oltmanns, S. and Niethammer, U.: Optimising UAV topographic surveys processed with structure-from-motion: Ground control quality, quantity and bundle adjustment, Geomorphology, 280, 51-66, doi:10.1016/j.geomorph.2016.11.021, 2017.

Javernick, L., Brasington, J., and Caruso, B.: Modeling the topography of shallow braided rivers using Structure-from-Motion photogrammetry, Geomorphology, 213, 166–182, doi:10.1016/j.geomorph.2014.01.006, 2014.

Khan, N. I., and Islam, A.: Quantification of erosion patterns in the Brahmaputra–Jamuna River using geographical information system and remote sensing techniques, Hydrological Processes, 17(5), 959-966, doi: 10.1002/hyp.1173, 2003.

Kessler, A. C., Gupta, S. C., and Brown, M. K.: Assessment of river bank erosion in Southern Minnesota rivers post European settlement, Geomorphology, 201, 312-322, doi:10.1016/j.geomorph.2013.07.006, 2013.

Kimiaghalam, N., Goharrokhi, M., Clark, S. P., Ahmari, H.: A comprehensive fluvial geomorphology study of riverbank erosion on the Red River in Winnipeg, Manitoba, Canada, Journal of Hydrology, 529, 1488-1498, doi:10.1016/j.jhydrol.2015.08.033, 2015.

Lague, D., Brodu, N., and Leroux, J.: Accurate 3D comparison of complex topography with terrestrial laser scanner: Application to the Rangitikei canyon (NZ), ISPRS Journal of Photogrammetry and Remote Sensing, 82, 10-26, doi:10.1016/j.isprsjprs.2013.04.009, 2013.

Lane, S. N.: The measurement of river channel morphology using digital photogrammetry, The Photogrammetric Record, 16(96), 937-961, doi:10.1111/0031-868X.00159, 2000.

Lane, S.N., Widdison, P.E., Thomas, R.E., Ashworth, P.J., Best, J.L., Lunt, I.A., Sambrook Smith, G.H. and Simpson, C.J.: Quantification of braided river channel change using archival digital image analysis, Earth Surface Processes and Landforms, 35(8), 971-985, doi:10.1002/esp.2015, 2010.

Lawler, D. M.: Process dominance in bank erosion systems, Lowland floodplain rivers: Geomorphological perspectives, 117-43, 1992.

Lawler, D.M.: The measurement of river bank erosion and lateral channel change: a review, Earth surface processes and landforms, 18(9), 777-821, doi:10.1002/esp.3290180905, 1993.

Lawler, D.M.: The importance of high-resolution monitoring in erosion and deposition dynamics studies: examples from estuarine and fluvial systems, Geomorphology, 64(1), 1-23, doi:10.1016/j.geomorph.2004.04.005, 2005.

Leyland, J., Darby, S. E., Teruggi, L., Rinaldi, M., and Ostuni, D.: A self-limiting bank erosion mechanism? inferring temporal variations in bank form and skin drag from high resolution topographic data, Earth Surf. Process. Landforms, 40: 1600–1615, doi:10.1002/esp.3739, 2015.

Massey, D.: Talking of space-time, Transactions of the Institute of British Geographers, 26: 257–261, doi:10.1111/1475-5661.00019, 2001.

45

Micheletti, N., Chandler, J. H., and Lane, S. N.: Investigating the geomorphological potential of freely available and accessible structure-from-motion photogrammetry using a smartphone, Earth Surface Processes and Landforms, 40(4), 473-486, doi:10.1002/esp.3648, 2015.

Nardi, L., Campo, L., and Rinaldi, M.: Quantification of riverbank erosion and application in risk analysis, Nat Hazards, 69(1), 869-887, doi:10.1007/s11069-013-0741-8, 2013.

O'neal, M. A., and Pizzuto, J. E.: The rates and spatial patterns of annual riverbank erosion revealed through terrestrial laser-scanner surveys of the South River, Virginia, Earth Surface Processes and Landforms, 36(5), 695-701, doi:10.1002/esp.2098, 2011.

Ortuño, M., Guinau, M., Calvet, J., Furdada, G., Bordonau, J., Ruiz, A., and Camafort, M.: Potential of airborne LiDAR data analysis to detect subtle landforms of slope failure: Portainé, Central Pyrenees, Geomorphology, 295, 364-382, doi:10.1016/j.geomorph.2017.07.015, 2017.

Ouédraogo, M. M., Degré, A., Debouche, C., and Lisein,J.: The evaluation of unmanned aerial system-based photogrammetry and terrestrial laser scanning to generate DEMs of agricultural watersheds, Geomorphology, 214, 339–355, doi:10.1016/j.geomorph.2014.02.016, 2014.

Parker, G., Shimizu, Y., Wilkerson, G. V., Eke, E. C., Abad, J. D., Lauer, J. W., Paola, C., Dietrich, W. E., Voller, V. R.: A new framework for modeling the migration of meandering rivers, Earth Surface Processes and Landforms, 36(1), 70-86, doi:10.1002/esp.2113, 2011.

Passalacqua, P., Belmont, P., Staley, D.M., Simley, J.D., Arrowsmith, J.R., Bode, C.A., Crosby, C., DeLong, S.B., Glenn, N.F., Kelly, S.A. and Lague, D.: Analyzing high resolution topography for advancing the understanding of mass and energy transfer through landscapes: A review, Earth-Science Reviews, 148, 174-193, doi:10.1016/j.earscirev.2015.05.012, 2015.

Pyle, C. J., Richards, K. S., and Chandler, J. H.: Digital photogrammetric monitoring of river bank erosion, The Photogrammetric Record, 15(89), 753-764, doi:10.1111/0031-868X.00083, 1997.

Prosdocimi, M., Calligaro, S., Sofia, G., Dalla Fontana, G., and Tarolli, P.: Bank erosion in agricultural drainage networks: new challenges from structure-from-motion photogrammetry for post-event analysis, Earth Surface Processes and Landforms, 40(14), 1891-1906, doi:10.1002/esp.3767, 2015.

Reneau, S.L., Drakos, P.G., Katzman, D., Malmon, D.V., McDonald, E.V., Ryti, R.T.: Geomorphic controls on contaminant distribution along an ephemeral stream. Earth Surface Processes and Landforms, 29(10):1209-23, DOI: 10.1002/esp.108, 2004.

Resop, J. P., and Hession, W. C.: Terrestrial laser scanning for monitoring streambank retreat: Comparison with traditional surveying techniques, Journal of Hydraulic Engineering, 136(10), 794-798, doi:10.1061/(ASCE)HY.1943-7900.0000233, 2010.

Rhoades, E. L., O'Neal, M. A., and Pizzuto, J. E.: Quantifying bank erosion on the South River from 1937 to 2005, and its importance in assessing Hg contamination, Applied Geography, 29(1), 125-134, doi:10.1016/j.apgeog.2008.08.005, 2009.

Rinaldi, M., and Darby, S. E.: Modelling river-bank-erosion processes and mass failure mechanisms: progress towards fully coupled simulations, Developments in Earth Surface Processes, 11, 213-239. doi:10.1016/S0928-2025(07)11126-3, 2008.

Rinaldi, M., Casagli N., Dapporto S., and Gargini, A.: Monitoring and modeling of pore water pressure changes and riverbank stability during flow events, Earth Surf. Processes Landforms, 29, 237–254, doi: 10.1002/esp.1042, 2004.

5   Siviglia, A., & Crosato, A.: Numerical modelling of river morphodynamics: Latest developments and remaining challenges. Advances in Water Resources, 93(A), 1-3, doi:10.1016/j.advwatres.2016.01.005, 2016.

Slatton, K. C., Carter W. E., Shrestha R. L., and Dietrich W.: Airborne Laser Swath Mapping: Achieving the resolution and accuracy required for geosurficial research, Geophys. Res. Lett., 34, L23S10, doi:10.1029/2007GL031939, 2007.

Smith, M. W., Carrivick, J. L., Hooke, J., and Kirkby, M. J.: Reconstructing flash flood magnitudes using "Structure-from-
10   Motion": A rapid assessment tool, J. Hydrol., 519, 1914–1927, doi:10.1016/j.jhydrol.2014.09.078, 2014.

Snavely, N., Seitz, S. M., and Szeliski, R.: Modeling the world from internet photo collections, International Journal of Computer Vision, 80(2), 189-210, doi:10.1007/s11263-007-0107-3, 2008.

Spiekermann, R., Betts, H., Dymond, J., and Basher, L.: Volumetric measurement of river bank erosion from sequential historical aerial photography, Geomorphology, 296, 193-208, doi:10.1016/j.geomorph.2017.08.047, 2017.

15   Tamminga, A. D., Brett C. E., and Hugenholtz C. H.: UAS-based remote sensing of fluvial change following an extreme flood event, Earth Surface Processes and Landforms 40, no. 11, 1464-1476, doi: 10.1002/esp.3728 , 2015.

Tarolli, P., Sofi,a G., Dalla Fontana, G.: Geomorphic features extraction from high-resolution topography: landslide crowns and bank erosion, Natural Hazards, 61(1), 65-83, doi:10.1007/s11069-010-9695-2, 2012.

Telling, J., Lyda, A., Hartzell, P., and Glennie, C.: Review of earth science research using terrestrial laser scanning, Earth-
20   Science Reviews, 169, 35-68, 10.1016/j.earscirev.2017.04.007, 2017.

Thoma, D. P., Gupta, S. C., Bauer, M. E., and Kirchoff, C. E.: Airborne laser scanning for riverbank erosion assessment, Remote sensing of Environment, 95(4), 493-501, doi:10.1016/j.rse.2005.01.012, 2005.

Thorne, C. R.: Processes and mechanisms of river bank erosion, Gravel-bed rivers, 227-259, 1982.

Thorne, C.R. and Tovey N.K.: Stability of composite river banks, Earth Surface Processes and Landforms, 6(5), 469-484,
25   doi:10.1002/esp.3290060507, 1981.

Tonkin, T. N., Midgley, N. G., Graham, D. J., and Labadz, J. C.: The potential of small unmanned aircraft systems and structure-frommotion for topographic surveys: A test of emerging integrated approaches at Cwm Idwal, North Wales, Geomorphology, 226, 35–43, doi:10.1016/j.geomorph.2014.07.021, 2014.

Turner, D., Lucieer, A., and de Jong, S.: Time Series Analysis of Landslide Dynamics Using an Unmanned Aerial Vehicle
30   (UAV), Remote Sensing, 7, 1736–1757, doi:10.3390/rs70201736, 2015.

Westoby, M. J., Brasington, J., Glasser, N. F., Hambrey, M. J., and Reynolds, J. M.: 'Structure-from-Motion' photogrammetry: A low-cost, effective tool for geoscience applications, Geomorphology, 179, 300-314, doi:10.1016/j.geomorph.2012.08.021, 2012.

Woodget, A. S., Carbonneau, P. E., Visser, F., and Maddock, I. P.: Quantifying submerged fluvial topography using hyperspatial resolution UAS imagery and structure from motion photogrammetry, Earth Surf. Proc. Land., 40, 47–64, doi:10.1002/esp.3613, 2015.

Table 1. Number of photographs and overlaps for the tests

	Test 1a	Test 1b	Test 1c	Test 1d	Test 2	Test 3	Test 4	Test 5
Track 1	293	147	73	37		147		293
Track 2					232	232		232
Track 3							232	232
Track 4							232	232
Min. overlaps	16	8	4	2	7	15	26	49
Max. overlaps	20	10	5	2	7	17	26	53

Table 2. Mean and standard deviation of elevation differences between SfM DSMs and GPS points. Colour intensity indicates the deviation from zero value with minimum/maximum of ±0.13 m.

Surface	Error (m)	Test 1a	Test 1b	Test 1c	Test 1d	Test 2	Test 3	Test 4	Test 5
All grounds	Mean	-0.01	0.00	0.00	0.04	0.03	-0.01	-0.05	0.00
-	Std. dev.	0.03	0.03	0.04	0.07	0.03	0.03	0.05	0.03
Grassland	Mean	0.02	0.01	0.01	0.02	0.02	0.01	0.01	0.02
-	Std. dev.	0.03	0.03	0.04	0.04	0.03	0.02	0.02	0.02
Bank	Mean	0.00	0.01	-0.01	-0.01	0.05	0.01	-0.03	0.01
-	Std. dev.	0.04	0.03	0.07	0.13	0.03	0.03	0.04	0.03
Terrace	Mean	-0.02	-0.02	0.00	0.06	0.03	-0.02	-0.09	-0.01
-	Std. dev.	0.02	0.03	0.03	0.06	0.03	0.02	0.03	0.02

5

Table 3. Mean and standard deviation of elevation differences between SfM, ALS and RTK GPS. Colour intensity indicates the deviation from zero value with minimum/maximum of ±0.09 m.

Subtraction	-	All grounds	Grassland	Bank	Terrace
SfM - ALS (m)	Mean	-0.01	0.01	-0.06	-0.04
	Std. dev.	0.03	0.02	0.06	0.03
ALS - GPS (m)	Mean	0.01	0.01	0.01	0.01
	Std. dev.	0.05	0.03	0.09	0.05
SfM - GPS (m)	Mean	-0.01	0.01	0.01	-0.02
	Std. dev.	0.03	0.02	0.03	0.02

5